

# JGR Solid Earth



## RESEARCH ARTICLE

10.1029/2022JB026019

# Pressure Solution Grain Boundary Sliding as a Large Strain Mechanism of Superplastic Flow in the Upper Crust

Jean-Pierre Gratier<sup>1,2</sup> , Luca Menegon<sup>3</sup> , and François Renard<sup>1,3</sup> 

<sup>1</sup>ISTerre, University Grenoble Alpes, Grenoble INP, University Savoie Mont Blanc, CNRS, IRD, University Gustave Eiffel, Grenoble, France, <sup>2</sup>Honorary Professor of the University Grenoble Alpes, Grenoble, France, <sup>3</sup>The Njord Centre, Departments of Geosciences and Physics, University of Oslo, Oslo, Norway

### Key Points:

- During the Alpine orogeny, calcareous shales transformed to slate schists accommodated large ductile deformation at shallow depth (5–8 km)
- Microstructural studies reveal near-equant fine grains and mass transfers implying grain-boundary sliding mechanism in superplastic flow
- Modeled deformation maps show that diffusive mass transfer properties may be slower in nature than in laboratory experiments

### Correspondence to:

J.-P. Gratier,  
[jeanpierre.gratier@gmail.com](mailto:jeanpierre.gratier@gmail.com)

### Citation:

Gratier, J.-P., Menegon, L., & Renard, F. (2023). Pressure solution grain boundary sliding as a large strain mechanism of superplastic flow in the upper crust. *Journal of Geophysical Research: Solid Earth*, 128, e2022JB026019. <https://doi.org/10.1029/2022JB026019>

Received 10 NOV 2022  
Accepted 7 MAR 2023

### Author Contributions:

**Conceptualization:** Jean-Pierre Gratier  
**Methodology:** Jean-Pierre Gratier, Luca Menegon, François Renard  
**Validation:** Luca Menegon, François Renard  
**Writing – original draft:** Jean-Pierre Gratier  
**Writing – review & editing:** Luca Menegon, François Renard

**Abstract** A mechanism accommodating large strain in superplastic flow with elongation of 100%–300%, is described for fine-grained calcareous shales deformed at temperature of 200–335°C and depths of 5–8 km up to slate schists in the Oisans massif, Western Alps, France. Using electron microscopy techniques on thin sections parallel to the principal finite strain axes, we show that the shape ratios of the slightly elongated grains (1.4–1.6), mainly calcite and quartz, do not match the finite strains recorded by the markers of the deformation (truncated belemnites, folded veins) in the maximum elongation and shortening plane (ratio 6.7) or in the maximum and minimum elongations plane (ratio 2.4). Consequently, a grain boundary sliding mechanism is required to explain the measured large finite strains. The most soluble minerals (quartz, calcite, dolomite, and albite), which represent about 95% of the rock, accommodate deformation by pressure solution grain boundary sliding whereas the least soluble minerals (muscovite, chlorite, Fe-Ti oxides) act as indenters or are passively reoriented. Pressure solution is especially efficient in polymineralic rocks. Soluble minerals, which have been healed together in veins or fossils, are much more resistant to deformation and act as rigid objects. Models with idealized tessellation of hexagonal grains and creep laws derived from pressure solution indentation experiments provide deformation maps. We discuss the main parameters of this ductile deformation in the upper crust (thermodynamic conditions, strain rate, stress, distance of mass transfer) and show possible drastic decrease of mass transfer efficiency with decrease of stress and strain rate.

**Plain Language Summary** The formation of mountain ranges such as the Alps is associated with large strain flow of fine-grained rocks even at low temperatures (200–335°C) and shallow depths (5–8 km). Such ductile behavior represents an aseismic alternative (without earthquakes) in highly deformed zones, so it is important to understand and model it in order to predict the mechanical behavior of actively deforming regions. However, the mechanism and the parameters of the deformation remain enigmatic. Relying on grain shape analyses derived from microscopy techniques, we demonstrate that the deformation is accommodated by grain boundary sliding with locally stress-driven dissolution in zones that oppose grain sliding and re-deposition in zones that are stress-relaxed by this sliding. By comparison with laboratory experiments, we show that this ductile process may operate in fine-grained rocks, at much lower stresses than required for seismic deformation. We establish flow laws that describe the relation between strain rate and the parameters of the deformation, such as thermodynamic conditions, stress, distance and characteristics of mass transfer along grain boundaries. We show that, at low differential stress and slow strain rate, diffusive mass transfer along grain boundaries could be much slower than when measured in laboratory experiments at high stress and strain rate.

## 1. Introduction

Rocks deformed under very high strains in the elongation range of 100%–300% and shortening of 50%–75% are commonly observed in mountains and continental shear zones that have recorded crustal deformations (Pfiffner & Ramsay, 1982). In order to better quantify the strain - stress relationships (i.e., creep laws) associated with such ductile deformations, it is crucial to better understand the deformation mechanisms at the grain scale (Poirier, 1985).

Faced with the challenge of understanding the deformation mechanism of experimentally highly deformed polycrystalline synthetic materials, with characterized behavior of superplastic flow (Ashby & Verral, 1973), proposed a model of grain boundary sliding where diffusion accommodates deformation. In dislocation creep, Nabarro-Herring creep or Coble creep, the grains accommodate the same amount of deformation as the material

© 2023. The Authors.

This is an open access article under the terms of the [Creative Commons Attribution License](https://creativecommons.org/licenses/by/4.0/), which permits use, distribution and reproduction in any medium, provided the original work is properly cited.

on a whole and keep the same neighbors. Conversely, in the grain boundary sliding model, the grains remain nearly equant and switch their neighbors with diffusion-accommodated flow (Ashby & Verral, 1973). In this model, grain boundary sliding is controlled both by bulk and grain boundary solid diffusion, the latter being most often dominant. This model also considers the possible effect of dislocation creep in the change of shape, mainly at high stress levels and accounts for the transition from dominant diffusion accommodated flow to dominant dislocation creep.

Application to natural deformation in the context of relatively high temperature has been proposed by (Boullier and Guéguen, 1975), who suggested six conditions and observations for the development of diffusion-accommodated superplasticity in natural mylonites: (a) high temperature:  $T/T_m > 0.5$  where  $T_m$  is the melting temperature, (b) permanent small grain size (less than 10 microns) and nearly equant grains, (c) stress and strain rate not too high, to avoid dislocation-controlled plastic flow, (d) no crystallographic preferred orientation, (e) moderate dislocation densities, (f) relatively high strain rate sensitivity with low stress exponent. Diffusion-accommodated superplastic flow has been described both in lower crust (Behrmann & Mainprice, 1987) and mantle deformation (Hiraga et al., 2010). The absence of preferred crystallographic orientation or the low density of dislocations are not systematically observed in experiments of superplasticity on natural minerals at 700–900°C (Rutter et al., 1994; Rybacki et al., 2010; Schmid et al., 1977) indicating that a limited part of the deformation may be accommodated by dislocation creep or by preferential grain growth (Kamb, 1959; Paterson, 1990) at least in the relatively high experimental strain rate regime.

By extrapolating experimental data to natural deformation (Paterson, 1990), reviewed how superplastic flow may occur under geological conditions in calcite, quartz and olivine rocks at relatively high temperature ( $T/T_m > 0.5$ ). He also noted that knowledge of superplasticity in most naturally deformed rocks is still incomplete, especially when a fluid phase is involved, such as in porous rock deformation. This is especially true for large strains observed in the upper crust at temperatures much lower than those required for efficient diffusion through solid in volume or at grain boundary (see above). In such cases, stress-driven mass transfer process, such as pressure solution creep with diffusion along fluid phase trapped under stress along grain boundaries, is a very efficient mechanism that can occur at the grain scale in natural deformation (Elliott, 1973). This mechanism may also involve local reequilibration by coupled dissolution and precipitation processes (Putnis & Putnis, 2007; Ruiz-Agudo et al., 2014) not discussed here. Pressure solution creep has been reproduced in the laboratory under pressure and temperature conditions representative of the upper crust down to 10–20 km of depth (e.g., Gratier, Dysthe, & Renard, 2013, and references therein, with some experiments specifically on calcite and quartz such as (Croizé et al., 2010; Gratier et al., 2009; Zhang et al., 2010). However, in most geological cases, multiphase materials have to be considered including minerals of various solubilities, consequently of various mobilities under stress. Modeling interface diffusion creep of such a multiphase material appears to be challenging (Ford & Wheeler, 2004). Another approach developed for quartz - illite aggregates is to consider combined effects of shearing friction process controlled by the illite phyllosilicates and of dilatant process controlled by quartz pressure solution (Bos et al., 2000; den Hartog and Spiers, 2014; Niemeijer & Spiers, 2007). This process strongly depends on temperature and strain rate with evolution from velocity strengthening behavior associated with creeping processes at high temperature or low strain rate to velocity weakening behavior associated with earthquake development at low temperature or fast strain rate. Consequently, it is of crucial interest to evaluate the shape and geometric orientation of each type of minerals. Depending on the mineral solubility and its crystallographic orientation, one can determine the parameters for deformation modeling and the relative contribution of diffusion creep, friction, and dislocation creep mechanisms, which accommodate large strain.

An example of large natural ductile deformation in the upper crust, in which the large strain values and the conditions of temperature and pressure are well known, is presented here. Based on detailed field observations in highly deformed Mesozoic basins in the Western Alps, we have selected one highly deformed representative sample. From this sample, we measured various parameters, including grain shape and grain shape orientation, and crystallographic preferred orientation. We compared it with less deformed rocks of the same type. We infer the occurrence of stress-driven mass transfer using various chemical and mineralogical analyses using SEM-EDS (Scanning Electron Microscopy/Energy Dispersive X-Ray Spectroscopy) and EBSD (Electron Back Scattered Diffraction) methods. These parameters depend on mineral solubility and on the characteristics of grain boundaries. The study allows proposing a mechanism of grain boundary sliding for superplastic behavior in large strain and a flow law controlled by pressure solution at relatively low temperature deformation and slow strain rate in the upper crust. Moreover, we show that some parameters, such as the characteristics of mass transfer (diffusion

coefficient, width of grain boundary) that are evaluated in laboratory experiments always conducted at high differential stress values and strain rate, have to be significantly scaled down when used in the low stress, slow strain rate natural conditions.

## 2. Geological Context

During the Alpine orogeny in Europe part of the Mesozoic cover of the Paleozoic basement has been locally highly deformed at relatively low temperature and pressure conditions (i.e., 5–8 km depth). This is the case for the sedimentary basins of the Oisans massif, France, which has been highly deformed and transformed from shales to slate schists in the context of the thrusting of the external crystalline alpine massifs (Figures 1a and 1b). In the Bourg d'Oisans basin (Figure 1c), large strain was accommodated by folds with slaty cleavage ( $S1$ ) along the axial plane, and internal deformation that can be determined from the shortening measured along ptygmatic folded veins (Ramsay, 1967) and truncated belemnite fossils for the elongation (Badoux, 1963) (Figures 1d and 1e). The intensity of deformation increases from east to west in the Bourg d'Oisans basin, associated with tightening of the folds. The fold shape evolution may be seen on the cross sections of Figure 1c and on the photographs of Figures 2a and 2b.

In the following, we define  $l_o$  as the initial length and  $l_x, l_y, l_z$  as the finite lengths in the principal directions of the finite deformation (Figure 1f). In the eastern part of the Bourg d'Oisans basin, the apparent gentle folds with axial plane cleavage show horizontal layer-parallel shortening  $l_z/l_o$  of about 0.5 with near vertical elongation of 2, locally deformed by basement thrusts with local crenulation cleavage ( $S2$ ) in the sedimentary cover (Figure 1c). In the central part, in the area of La Paute, finite strain values (Figure 1d1) are about 0.4 for horizontal shortening  $l_z/l_o$ , 2.5 for vertical elongation  $l_x/l_o$ , and 1.05 for the third horizontal principal strain  $l_y/l_o$ . In the western part, vertical elongations of more than 3 are measured west of la Paute with shortening of about 0.3 (Figure 1d2). Higher strain values are measured within some pinched basins in the Oisans massif, such as in the Côte Belle basin where vertical elongation ( $l_x/l_o$ ) is well above 4 and shortening ( $l_z/l_o$ ) is lower than 0.25 (Figure 1d3) (Gratier & Vialon, 1980). In summary, ratios of strain elongation to shortening range at least from 4 to 16. Not only the belemnite fossils have been truncated but also the fold axes have been progressively rotated during the deformation and reoriented to be near parallel to the elongation as sheath folds in the most deformed parts (Figure 1d1–2–3). Therefore, the whole sedimentary cover is affected by these large ductile deformations.

Temperature and confining pressure of the sedimentary cover of the Oisans massif have been estimated from thermopaleomagnetic record (Crouzet et al., 2001) coupled with K/Na geochronology on illite (Nziengui, 1993). A peak of metamorphism with temperature of 335°C, and pressure of 225 MPa (about 8.5 km depth) at 26.5 Ma was revealed, that rapidly decreased with time to 250°C at 23 Ma (corresponding to a geothermal gradient of 40°C/km), and then decreased more slowly to 180°C at 16.5 Ma. Confining pressure is linked to both the autochthonous sedimentary cover (2 km) and allochthonous pile of internal nappes up to 6 km thick. Shear displacement toward the west is revealed by the torsion of the axial plane folds in the upper part of the cover (Figure 1c).

At the grain scale, evidence of pressure solution creep is pervasively observed: quartz and calcite are locally dissolved in zones of maximum compressive stress near rigid objects and redeposited in veins, pressure shadows, and crystallization fillings in the voids between truncated belemnite elements (Gratier & Vialon, 1980). Studies of fluid inclusions in these redeposited minerals give detailed pressure-temperature relationships during deformation associated with slaty cleavage. Using the 40°C/km equivalent geothermal gradient, fluid inclusions data indicate a general decrease of temperature from 335 to 200°C (Bernard et al., 1977; Jenatton, 1981) corresponding to a maximum duration of 8 Ma at decreasing temperature (Crouzet et al., 2001). When studying specifically the fluid inclusions in crystallizations fillings of truncated belemnite fossil elements in the neighboring La Grave basin, Figure 1b (Jenatton, 1981), the temperatures range from 335 to 240°C corresponding to duration of 4 Ma at decreasing temperature, thereby covering a relatively large part of the total duration of the deformation. Deformation could be longer, maybe twice as long if it began during the first alpine shortening deformation in the basement at about 32 Ma according to (Bellanger et al., 2015), so the duration may range from about 4 to 16 Ma.

In order to best characterize the mechanism responsible for these large strains, one sample has been chosen in the La Paute area in the Liassic Sinemurian-Hettangian fine-grained calcareous shale formation (Barfety et al., 1972; Gidon, 1998). This sample contains a truncated belemnite fossil so that elongation may be perfectly measured and the shortening can be evaluated from nearby folded ptygmatic veins (Figures 1e and 1f). The aim of the

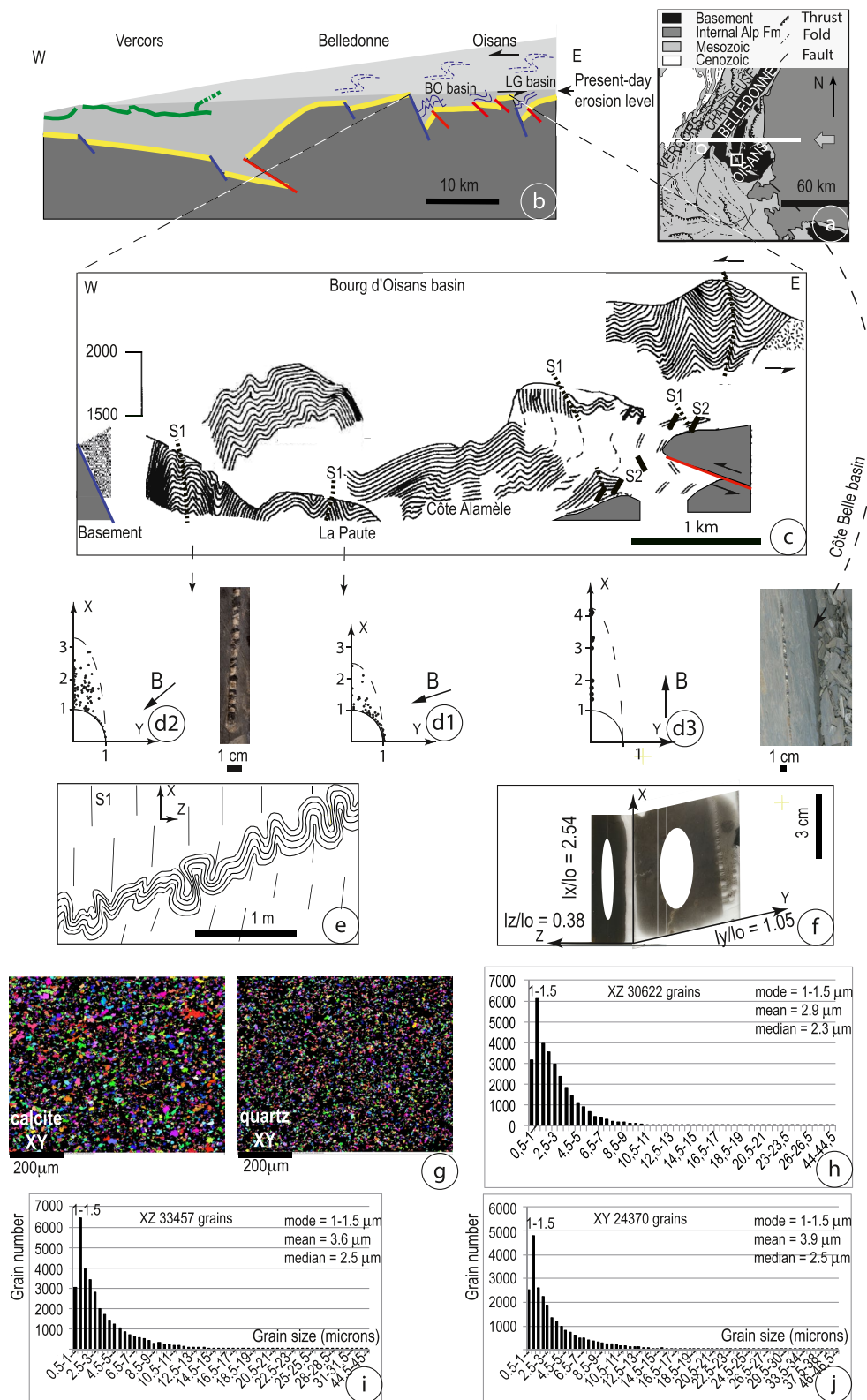
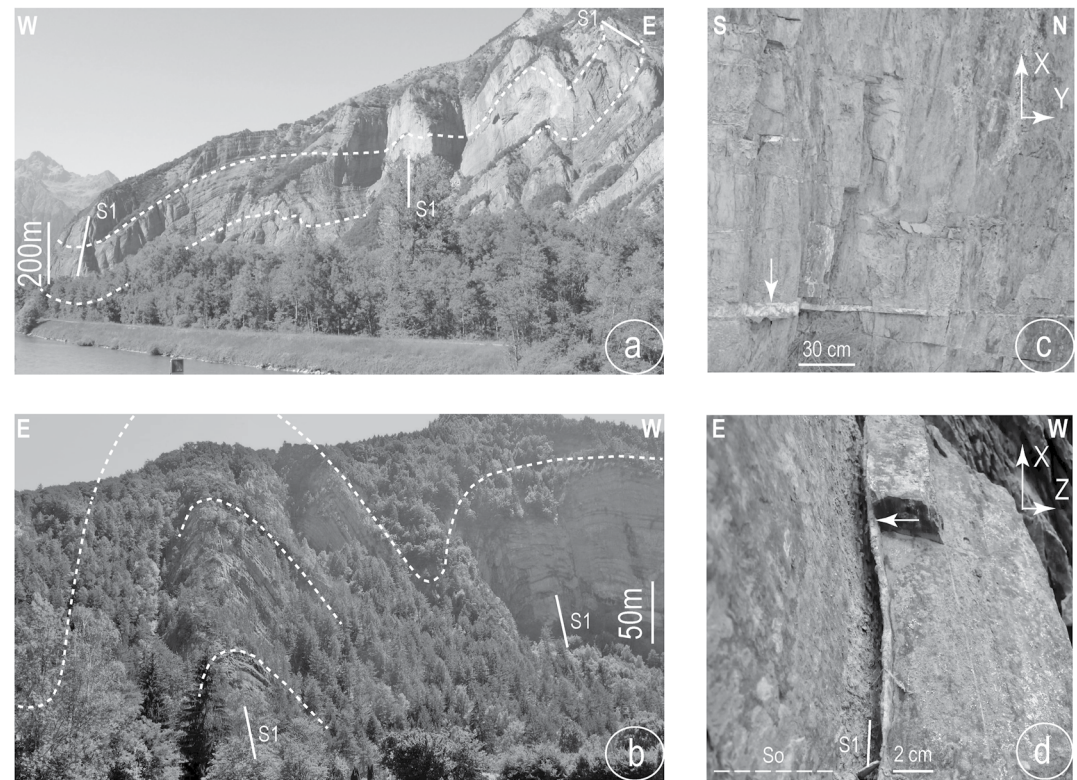


Figure 1.



**Figure 2.** Photographs of some key localities of the Bourg d'Oisans (BO) basin. Evolution of the tightening of the folds from the eastern part, the Côte Alamèle area (a) to the central part, the La Paute area (b). Folding is always associated with large internal finite deformation: E-W horizontal shortening increases from  $l_x/l_o = 2$  to 2.5 from eastern to central part respectively (Figure 1d1). (c) Large horizontal veins in the western part of the Bourg d'Oisans basin contributing to a very small part of the deformation (less than 0.01%) in a context of very large internal finite deformation: E-W shortening of 0.3, vertical elongation of 3.3 (Figure 1d2). The development of such veins at relatively low temperature (150°C deduced from fluid inclusion studies) marks the end of the superplastic deformation regime. (d) Boudinaged crystallization filling parallel to the vertical slaty cleavage and perpendicular to the horizontal strata in the La Paute area. This structure is possibly related to hydraulic fracturing episodes with opening of existing slaty cleavage and then deformation with the whole rock, with E-W shortening of 0.4 and vertical elongation of 2.5.

present study is to identify the mechanism of creep in the bulk rock associated with very large finite strain values with ratios of strain elongation over shortening ranging at least from 4 to 16, which could explain large ductile deformations observed in some shallow (<8 km depth) environments in the upper crust. In order to evaluate the evolution of grain size characteristics with the increase of deformation, EBSD analysis has also been performed on rock samples from a geological formation of the same age and characteristics of sedimentation (Gidon, 1998) in an area less deformed than the Bourg d'Oisans basin, and located to the west of the Oisans massif (Figures 1a, 1g and 1h).

**Figure 1.** Geological context of the study: (a) Structural map of the European Western Alps showing the pattern of folds and faults and the location of the general cross-section (white line), the horizontal arrows indicate the main shortening direction during Western Alps orogeny. (b) Schematic general cross-section with two reference formations: the Trias in yellow and the Urgonian (Cretaceous) in green, with the reconstructed thrust sedimentary cover over the Belledonne and Oisans massifs at the time of the deformation about 25 Ma ago (light gray). BO = Bourg d'Oisans, LG = La Grave. Major normal and thrust faults are indicated by blue and red lines respectively. (c) Elements of cross-section, through the Bourg d'Oisans basin, derived from photographs: calcareous shales have been folded with axial plane slaty cleavage (*S1*) and sheared in the upper part by the above thrusting of internal sedimentary cover and locally indented by basement thrust with associated *S2* crenulation cleavage. (d) Elongated truncated belemnite fossils: photographs and diagrams of elongation respectively for the western (d2), and middle part (d1) of the Bourg d'Oisans basin and for the Côte Belle basin (d3), location in (a), X-axis and Y-axis are the maximum elongation and the intermediate principal axes of the finite strain ellipsoid. B are the fold axes, photograph d3 from (Sechier, 2013). (e) Folded veins drawn from photograph where the Z-axis is the maximum shortening principal axis of the finite strain ellipsoid:  $l_z/l_o = 0.4$ . (f) The two studied thin sections along X-Z and X-Y planes with strain values (white ellipses) deduced from the truncated belemnite included in the X-Y thin section and from folded veins nearby. (g and h) EBSD maps of calcite and quartz and histogram of grain sizes of all the minerals in a rock sample from an area less deformed than the Bourg d'Oisans basin, and located to the west of the Oisans massif (circle on the geological map 1a). (i) & (j) Histogram of grain sizes of all the minerals cumulated for two areas within each of the two studied thin sections along X-Z and X-Y planes, with total grain numbers and mode, mean and median grain size values. Grain size derived from EBSD maps (Figures 3–5). Pixel size is 0.5  $\mu\text{m}$ .

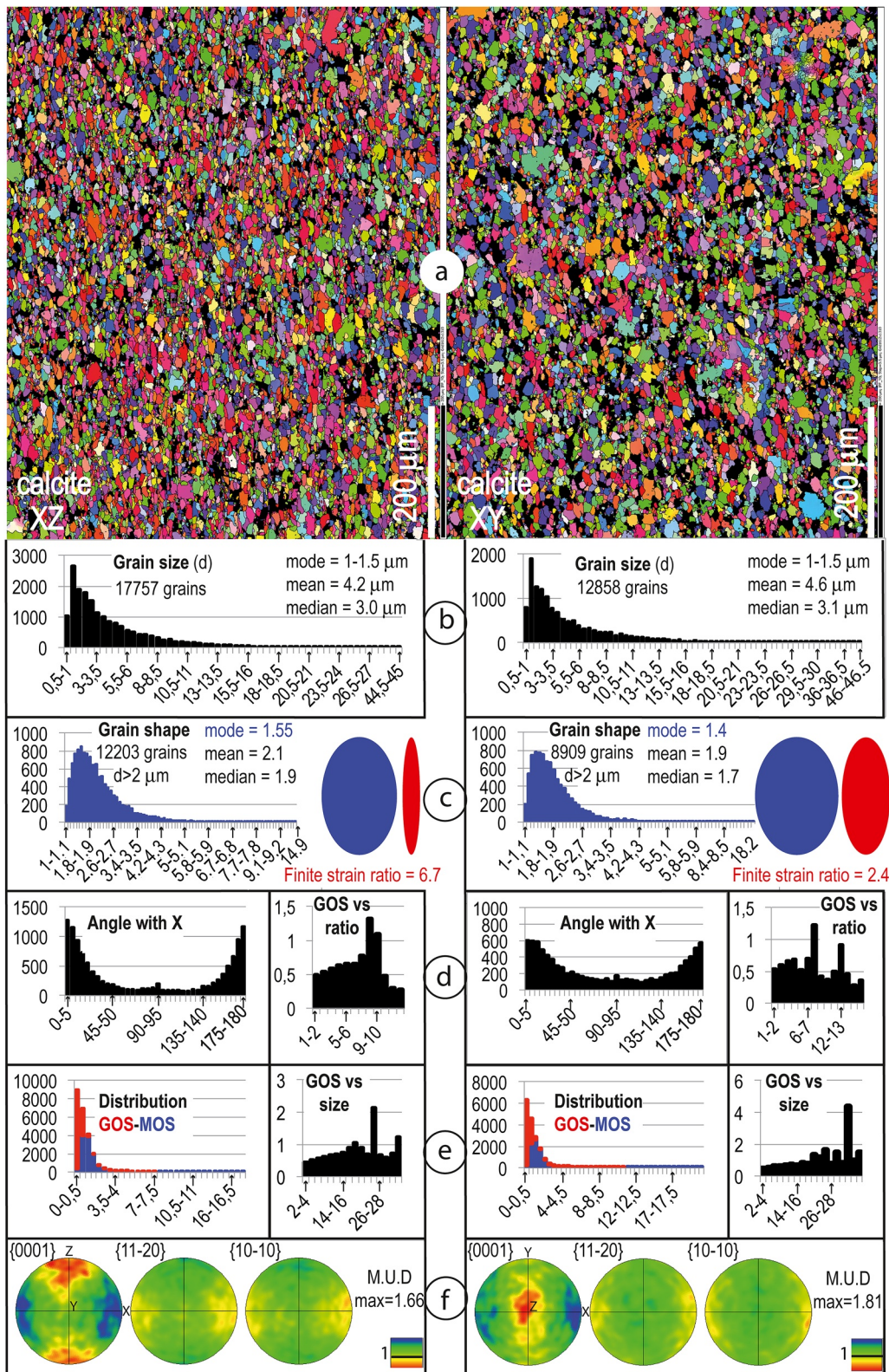


Figure 3.

### 3. Microstructural Analyses

#### 3.1. Sample Strain Measurements

At the sample scale (Figure 1f), elongation is calculated from the truncated belemnites by measuring the ratio between the finite length ( $l_x$ ) and the cumulated initial length of the truncated pieces of the fossil ( $l_o$ ). This ratio  $l_x/l_o$  shows a vertical elongation of 2.54 along the X-direction of maximum elongation. In the La Paute area horizontal elongation is measured along the horizontal intermediate Y-axis  $l_y/l_o$  and is small, equal to 1.05, Figure 1d1 (Gratier & Vialon, 1980). For the maximum shortening along the Z-axis, there are only some elements of pyramatic folded veins in the studied sample, but nearby in this part of the basin decimeter thick initially horizontal veins give various shortening values around  $0.04 \pm 0.05$ , Figure 1e. So assuming constant volume deformation at decimeters to meter scale (Bellanger et al., 2014)  $l_z/l_o$  could be here equal to 0.38. The ratio of principal finite strain values is thus 6.7 in the X-Z plane and 2.4 in the X-Y plane.

#### 3.2. Mineral Composition and Grain Deformation Characteristics

We characterized grain composition, microstructure and geometry by the EBSD technique using the CamScan X500 Crystal probe and the AZtec software (Oxford Instrument) at the University of Montpellier, France. Several areas have been investigated on the two thin sections parallel to the X-Z and X-Y principal finite strain axes: X-axis corresponds to the maximum elongation, Y-axis corresponds to the intermediate elongation and Z-axis corresponds to shortening (Figure 1f). Most analyses have been done with a pixel size of 0.5  $\mu\text{m}$  covering sites up to  $650 \times 800$  microns on several areas on both X-Z and X-Y sections. Analysis of more than 66,000 grains on nine sites for the two sections and using a combination of EBSD and element maps to estimate the phase abundances leads to the following weighted composition: calcite (82.9%), dolomite (2%) quartz (8.2%), muscovite (3.7%), chlorite (1%), albite (1.9%), apatite (0.2%), and pyrite (0.1%).

The central result of this analysis is the comparison between the grain geometry of the two X-Z and X-Y thin sections and the finite strain ellipses. Such comparisons are given for each main mineral: calcite (Figure 3), quartz (Figure 4) and muscovite (Figure 5) for the largest studied area on each section. Data on the other investigated areas show the same pattern. The grain size distribution is similar for the two sections with mode (1.25  $\mu\text{m}$ ), median (2.5  $\mu\text{m}$ ) and mean values (3.6 or 3.9  $\mu\text{m}$ ) for the X-Z and X-Y sections, respectively, with rare grain sizes up to 46  $\mu\text{m}$  (Figures 1i and 1j). The grain size distribution is also similar for the two perpendicular sections for each main mineral: 1.25  $\mu\text{m}$  for the maximum frequency mode in all cases, 4.2–4.6  $\mu\text{m}$  (calcite), 3–3.5  $\mu\text{m}$  (quartz), 1.6–1.8  $\mu\text{m}$  (muscovite) for mean values and 3–3.1  $\mu\text{m}$  (calcite), 2.5–2.9  $\mu\text{m}$  (quartz), 1.3–1.4  $\mu\text{m}$  (muscovite) for median values, respectively for X-Z and X-Y planes (Figures 3, 4b and 5b). Minor minerals have comparable sizes: albite has a similar grain size distribution as quartz, and pyrite and apatite are similar to muscovite.

A crucial parameter for deformation analysis is the length-to-width aspect ratio of the grains, which shows asymmetrical normal distributions with maximum frequency mode of 1.55, 1.65, and 2 for calcite (Figure 3), quartz (Figure 4), and muscovite (Figure 5), respectively, in the X-Z section, a value which is significantly lower than the measured finite strain ratio of 6.7 (Figure 1f). Moreover, despite the large difference in strain ratio from 6.7 in the X-Z plane to 2.4 in the X-Y plane, the mode values of the frequency distribution are only slightly different in the two sections X-Z and X-Y: for example, the difference for the mode values of the distribution is 1.55 to 1.4 for calcite, 1.65 to 1.5 for quartz, and 2 to 1.75 for muscovite for X-Z and X-Y sections, respectively. The mean values also differ only slightly: 2.1 to 1.9 for calcite, 2.4 to 2.1 for quartz, 3.2 to 2.7 for muscovite. Therefore, the shape of the grains does not reflect the shape of the real finite strain ellipses, requiring grain boundary sliding in order to accommodate large strains.

When analyzing the orientation of the grains, plots of the long axis versus the X-direction show a difference between the two sections for quartz and calcite grains with higher reorientation in the X-Z plane. An intriguing observation is that the muscovite grains (Figure 5d) have a lower degree of preferred orientation than the

**Figure 3.** Results of EBSD analysis of calcite grains on two perpendicular sections parallel to X-Z and X-Y planes, where X-axis is the maximum elongation, Z-axis is the maximum shortening, and Y-axis is the intermediate principal axis of the finite strain ellipsoid. (a) EBSD maps, pixel size = 0.5  $\mu\text{m}$ . (b) Histogram of grain sizes with total grain numbers and mode, mean, and median size values. (c) Histogram of grain shape values with analyzed number of grains larger than 2  $\mu\text{m}$  (for a good representativity due to the pixel size of 0.5  $\mu\text{m}$ ), with mode, mean and median size values, and comparison of the analyzed grain shape (blue) and the actual finite strain ellipse (red) deduced from strain markers (truncated belemnites and folded veins). (d-left) Distribution diagrams of the angles between the maximum grain elongation and the X-axis. (e-left) Distribution diagrams of the Grain Orientation Spread (GOS) and the Maximum Orientation Spread (MOS) relative to grain shape ratio. (d-right) Diagrams of GOS values relative to the grain shape ratio. (e-right) Diagrams of GOS values relative to the grain size. (f) Pole figures in equal area projection of lower hemisphere with maxima expressed as Multiple of Uniform Distribution (M.U.D.). The EBSD data are available on the NIRD Research Data Archive (Renard, 2022).

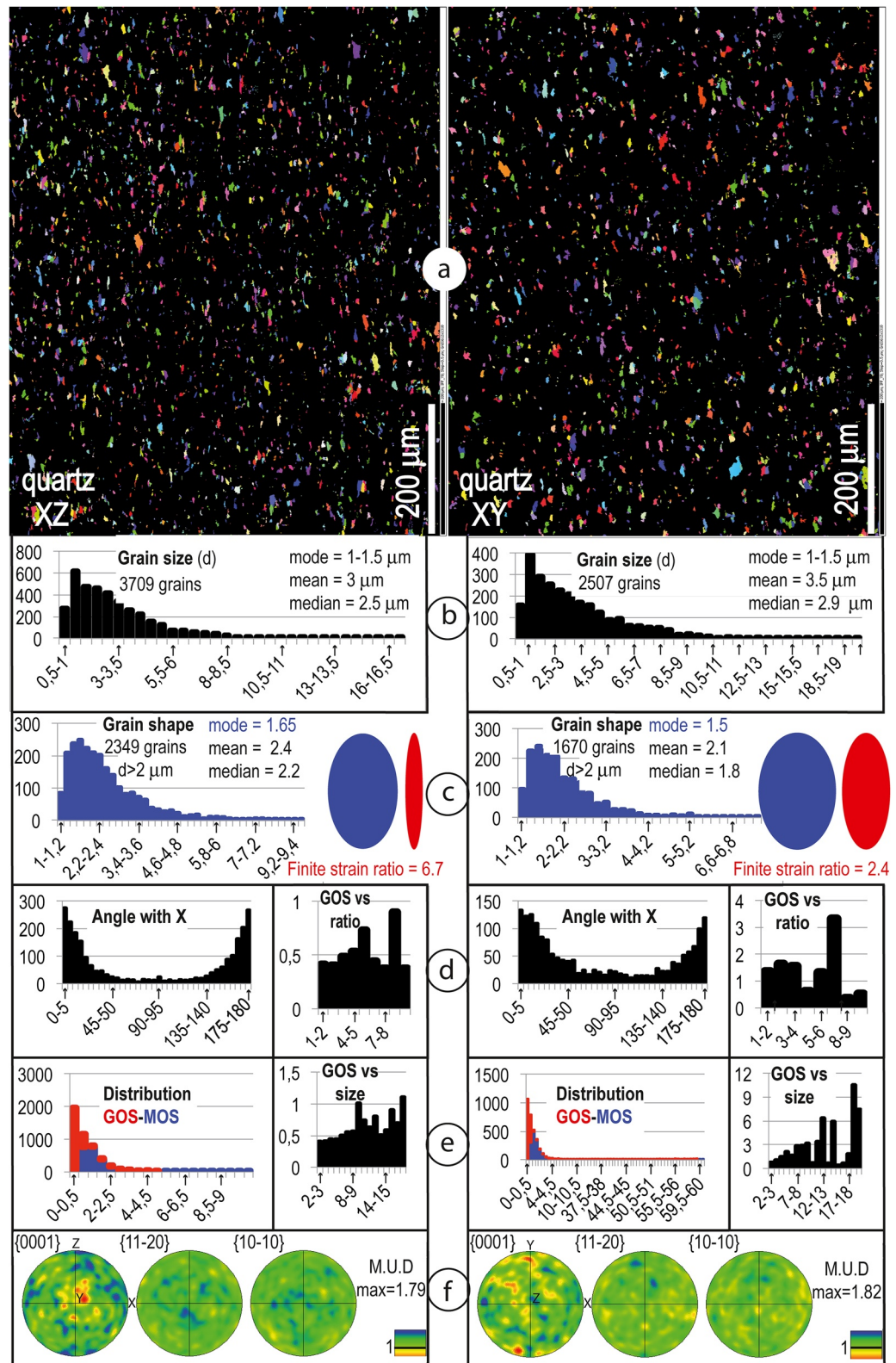


Figure 4. Results of EBSD analysis of quartz grains. Same caption as in Figure 3.

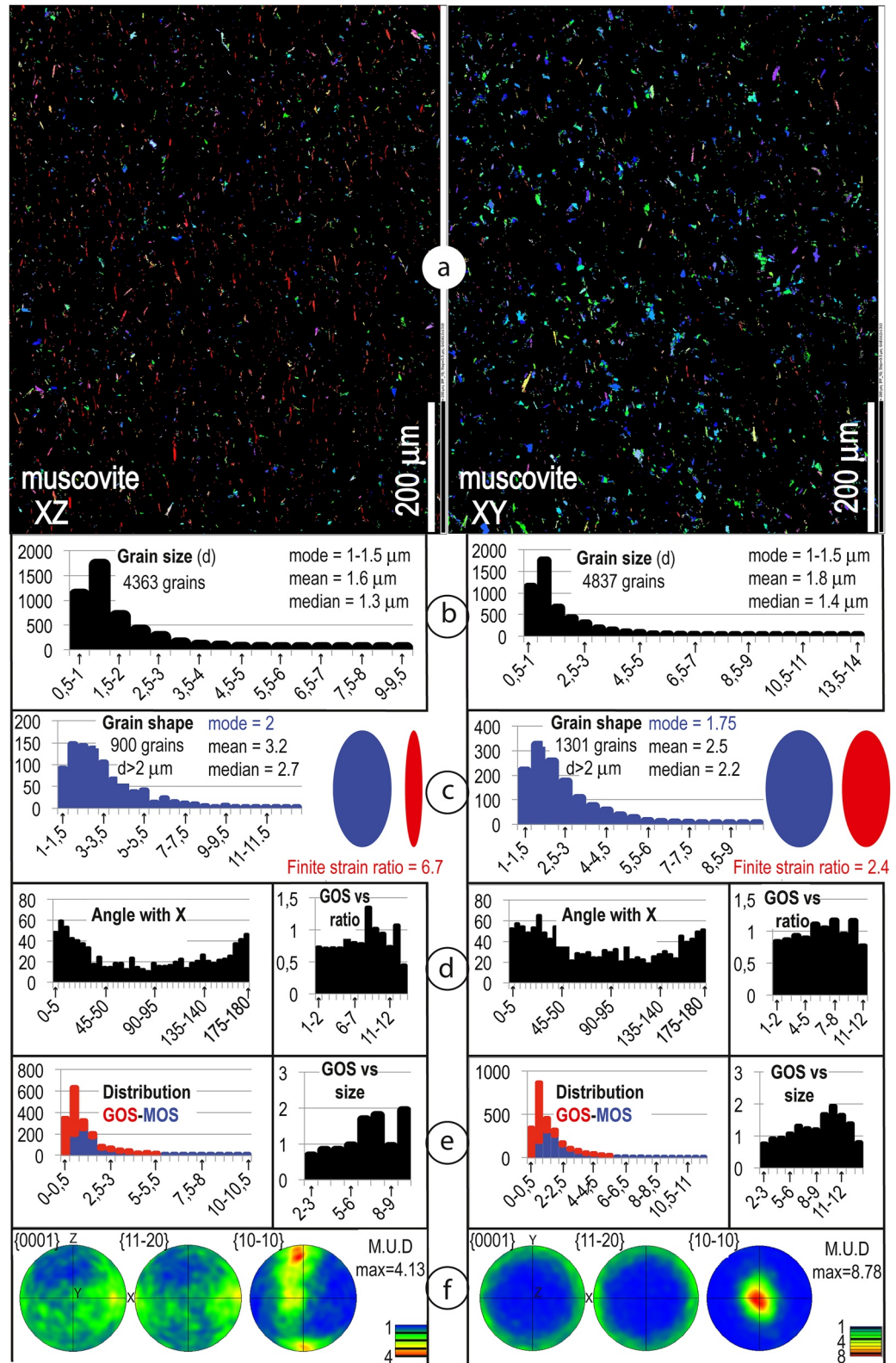


Figure 5. Results of EBSD analysis of muscovite grains. Same caption as in Figure 3.

calcite and quartz grains (Figures 3 and 4d). This result contradicts the common idea that these flat minerals are passively rotated during large strain.

Grain Orientation Spread (GOS) and Maximum Orientation Spread (MOS) distributions (Hielscher et al., 2022) representing the values of average and maximum internal misorientation (i.e., lattice distortion) of the grains, respectively, show a mode value of the frequency distribution of  $0^{\circ}$ – $0.5^{\circ}$  and  $1^{\circ}$ – $1.5^{\circ}$  for calcite and quartz, and  $0.5^{\circ}$ – $1^{\circ}$  and  $1^{\circ}$ – $1.5^{\circ}$  for phyllosilicates (Figures 3e, 4e and 5e). There is no systematic relationship between lattice distortion (expressed as GOS and MOS values) and strain ratio and size of grains. This indicates that grains of different sizes and with large or small strain ratio have all a very low internal lattice distortion (within  $1.5^{\circ}$ ) (Figures 3d and 3e, 4d and 4e, and 5d and 5e). Finally, the statistical description of the intensity of the fabric is quantified using the maximum intensity of the contoured pole figures and is given here as multiples of uniform distribution (M.U.D.). A weak crystallographic preferred orientation is observed on pole figures without a significant difference between the two areas on the two sections X-Z and X-Y, with a relatively low maximum of 1.66 and 1.79 M.U.D. for calcite and quartz respectively on section X-Z (Figures 3f and 4f), and of 1.81 and 1.82 M.U.D. on section X-Y. Maxima are a bit higher for phyllosilicates: 4.13 for section X-Z and 8.78 for section X-Y (Figure 5f).

### 3.3. Evidence of Stress-Induced Mass Transfer at the Grain Scale

Evidence of stress-driven mass transfer can be seen around relatively rigid undeformed objects such as pieces of folded veins (Figure 6a) and fossil fragments (Figure 6b). When comparing the chemical composition of the part of the rock matrix that has been exposed to maximum stress (by the indenting effect of the rigid object) with the part of the matrix that has been protected from stress in the pressure shadow of this rigid object, mass and volume changes can be calculated. Mineral contents are calculated from element maps (Figures 6 and 7). Results show that phyllosilicates (muscovite, chlorite) and Fe-Ti oxides are passively concentrated in the zones of maximum stress due to stress-driven dissolution of soluble minerals such as calcite, quartz, dolomite, albite in both examples noted a and b in Figure 6. The global change of mass transfer  $\Delta M/M_o$  is equal to  $(I_p/I_e - 1)$ ,  $I_p$  and  $I_e$  being the concentration of the insoluble minerals in the protected and exposed zones, respectively. The global mass variation is  $-0.66$  and  $-0.87$  for the two studied examples (Figures 6a and 6b). The relative decrease of mass of each soluble mineral,  $\Delta M_s/M_{so}$ , is equal to  $(I_p/I_e) (S_e/S_p) - 1$ ,  $S_e$  and  $S_p$  being the concentrations of the soluble minerals in the exposed and protected areas, respectively (Gratier, Dysthe, & Renard, 2013). These mass variations are equal to  $-0.95$  and  $-0.95$  for quartz and  $-0.75$  and  $-0.91$  for calcite for the two studied examples a and b, respectively (Figures 6a and 6b). Additional data on neighboring samples show that the local rock density is not significantly modified from protected to exposed zones indicating that the mass transfer may be equivalent to volume change. Therefore, such localized volume changes accommodate the heterogeneity of the deformation at the scale of some cluster of grains that appear to be relatively more rigid than the whole rock. It must be noted that paradoxically such undeformed objects are almost exclusively made of soluble minerals such as calcite (Figure 6). This is a general observation that, deformed under the same geometric and thermodynamics conditions; monomineralic rocks are more difficult to deform by pressure solution in natural deformation than polymineralic ones (Gratier, Thouvenot, et al., 2013). This is discussed below.

At the grain scale, we observe the clear indenting of the more soluble minerals such as quartz, calcite, and albite by the less soluble phyllosilicate minerals (Figure 7a). Local grain dissolution is observed as the dissolution of dolomite growth rings (Figure 7a). Evidence of calcite and quartz crystallization growth is also seen in the pressure shadows of these minerals (Figure 7b) or more rarely as discontinuous veins (Figure 7c). The microstructure of the grains evolves from a core with a high density of fluid inclusions to a more compact external part (Figure 7d).

As a conclusion of all these microstructural analyses when considered together, the most soluble minerals such as quartz, calcite, dolomite and albite, which represent about 95% of the rock mass, accommodate very large strains by pressure solution at grain boundaries whereas the least soluble minerals such as muscovite, chlorite and Fe-Ti oxides act as rigid indenters or are passively reoriented. Locally, some soluble minerals, which have been healed together in veins or fossils, are much more resistant to the pressure solution process and act as rigid objects.

## 4. Discussion

### 4.1. Characteristics of Superplastic Deformation From Microstructural Analyses

The first crucial observation is that grain shape does not reflect the finite strain ellipse in thin sections oriented in both X-Z and X-Y principal finite strain planes (Figures 3c, 4c, and 5c). The only way to explain the large measured

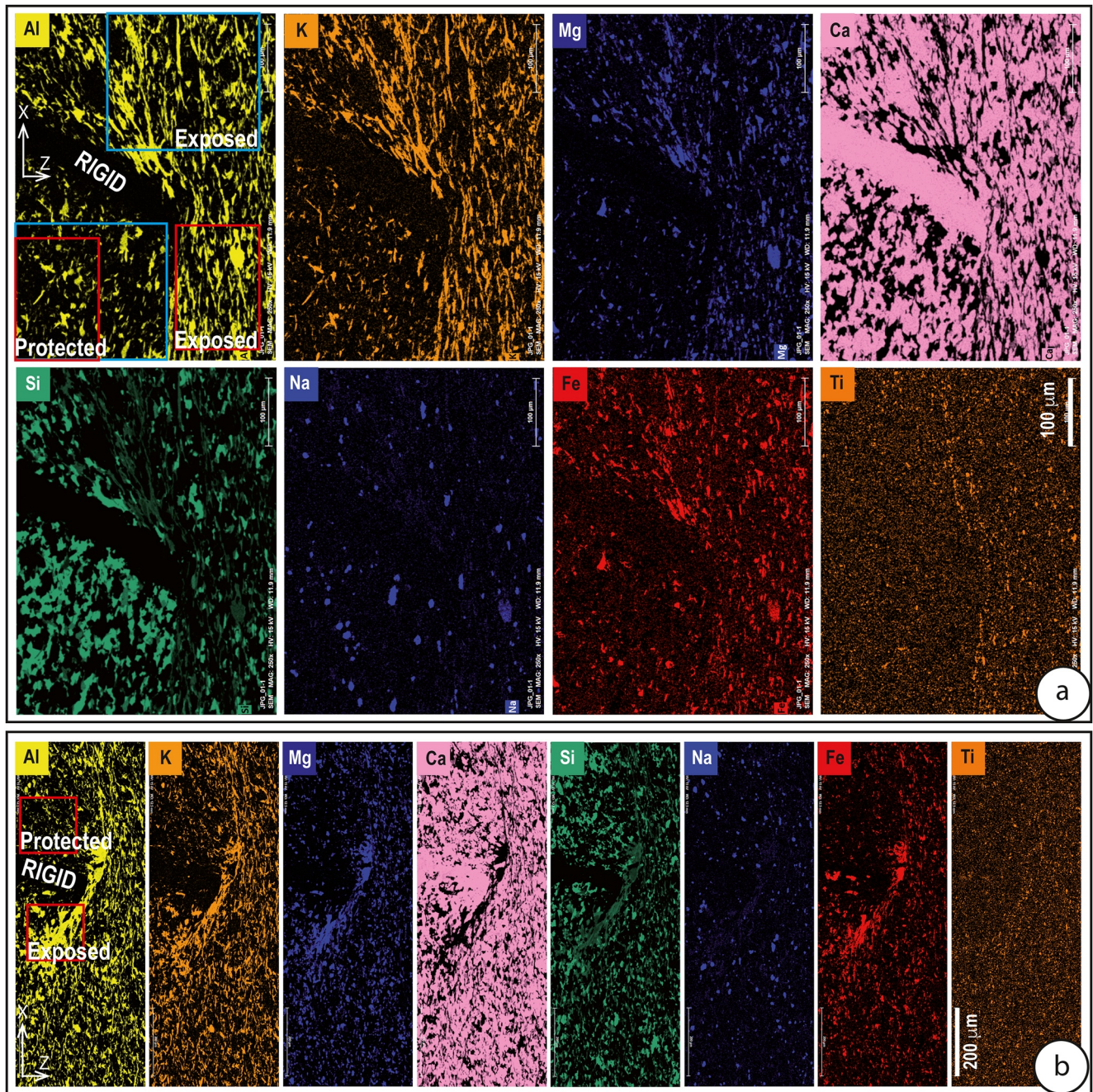


**Figure 6.** Element distribution maps from Scanning Electron Microscopy—Energy Dispersive Spectroscopy (SEM-EDS) showing stress-driven chemical differentiation between zones exposed to and protected from stress around rigid objects marked by the contrasting behavior of the minerals. Some minerals are dissolved under stress in the domain most exposed to stress, such as quartz (Si), calcite (Ca), dolomite (Ca-Mg) and albite (Si-Na) and other minerals are passively concentrated by this selective dissolution, such as muscovite (Si-Al-K), chlorite (Si-Al-Fe) and Ti-Fe oxides. Associated volume changes between various exposed and protected zones are estimated showing large volume decrease in the stress-exposed zones around rigid objects. These rigid objects are either a piece of folded vein (a) or piece of fossil (b), mainly composed of monomineralic well-healed calcite grains that do not allow stress-driven dissolution due to the difficulty of mass transfer along such well-healed grain boundaries. The global change of mass transfer  $\Delta M/M_o = (I_p/I_e - 1)$  is  $-0.66$  and  $-0.87$  for the two studied locations a and b, respectively (adding the two areas in a). Here,  $I_p$  and  $I_e$  are the concentrations of the insoluble minerals in the protected and exposed zones, respectively. The relative decrease of mass of each soluble mineral  $\Delta M_s/M_{so} = (I_p/I_e) (S_e/S_p) - 1$  is  $-0.95$  and  $-0.95$  for quartz and  $-0.75$  and  $-0.91$  for calcite for the two study examples a & b, respectively, where  $S_e$  and  $S_p$  are the concentrations of the soluble minerals in the exposed and protected areas, respectively.

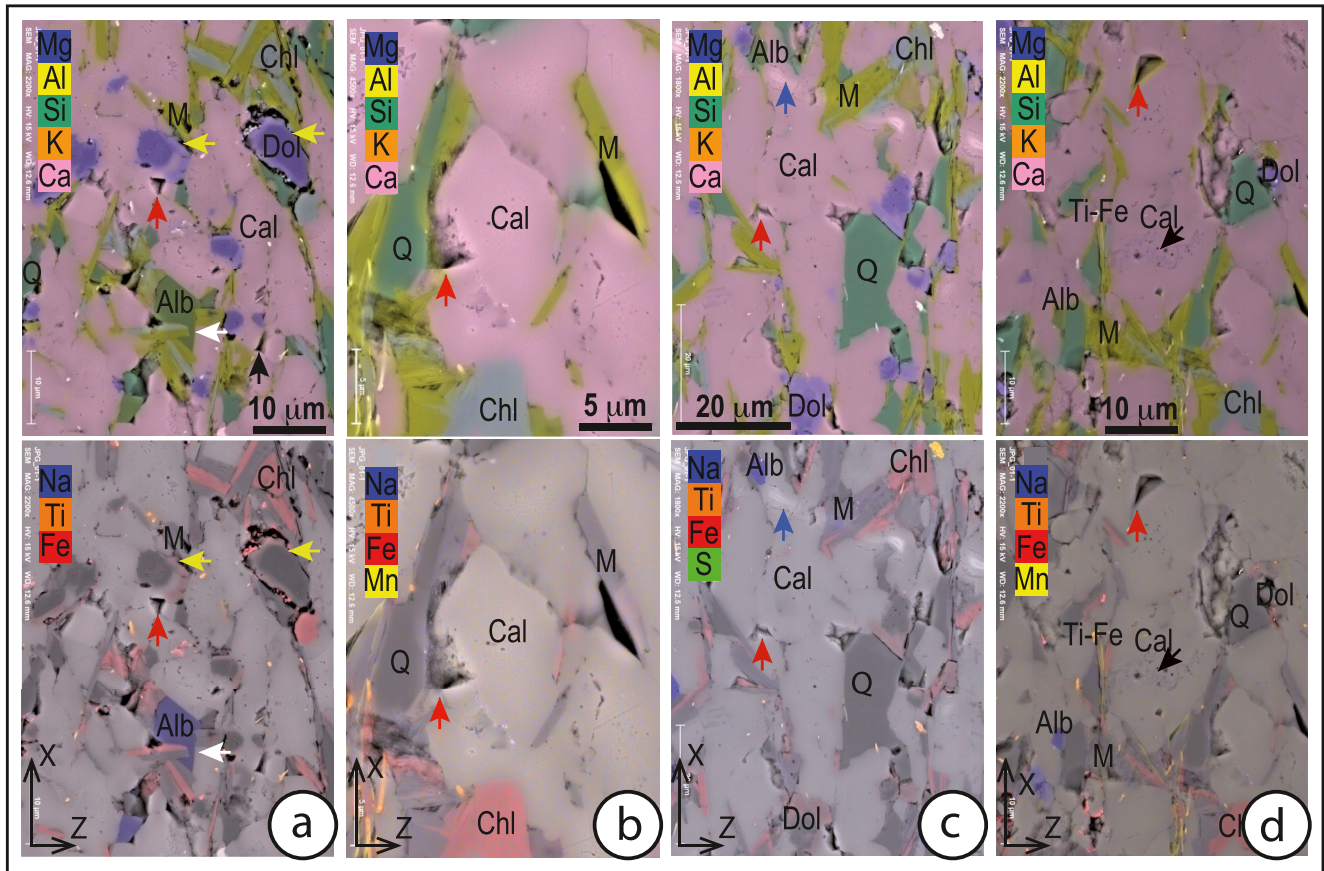


**Figure 7.** Microstructure of the deformed rock at the grain scale. The minerals are differentiated based on their element content: quartz (Q)-(Si), calcite (Cal)-(Ca), dolomite (Dol)-(Ca-Mg), albite (Alb)-(Si-Na), muscovite (M)-(Si-Al-K), chlorite (Chl)-(Si-Al-Fe), and titanium and iron oxides (Ti-Fe). Such polyminerals rocks with numerous unlike contacts (contact between different minerals) allow relatively easy mass transfer along grain boundaries that are not healed together through a pressure solution process. Evidence of stress-driven dissolution is seen thanks to the various Ca/Mg contents of growth rings of dolomite grains (yellow arrows) in (a) and to the indenting of some soluble minerals (Alb) by phyllosilicates (M & Chl), shown with white arrows in (a). Redeposition in voids between the grains are indicated by red arrows in (a–d). Mass transfer at grain scale is seen by heterogeneity in fluid inclusions content from the core to the periphery of some calcite grains and indicated by black arrows in (d). Very rare evidence of grain fracturing and healed veins may be seen and shown by a blue arrow in (c).

finite strain values is a mechanism of grain boundary sliding that accommodated the relative displacement of the grains. This mechanism has been described to explain large strains as superplastic flow, with diffusional accommodation of the grain boundary sliding, at relatively high temperature in the metal and geology communities (Ashby & Verral, 1973; Boullier and Guéguen, 1975; Schmid et al., 1977). In the sample studied here, fluids were present during the deformation, as indicated by fluid inclusions observed in redeposited minerals in veins, pressure shadows and in the space between truncated belemnite pieces (Bernard et al., 1977; Jenatton, 1981). The fluids allowed local intergranular mass transfer by pressure solution in the heterogeneously deformed zones around rigid objects (Figures 6a and 6b). These observations indicate that pressure solution creep is likely to be the main mechanism of mass transfer that accommodates grain boundary sliding. Under upper crust conditions, this mechanism is favored by the fact that diffusion efficiency in the water phase is much less dependent on the increase of temperature than diffusion in solid with about one order of magnitude of difference in the activation energy (15 kJ/mole for pressure solution, and up to 200 kJ/mole for solid state diffusion) (Rutter, 1976; Schmid et al., 1977). Pressure solution creep is strongly dependent on the geometry of the fluid phase along these grain boundaries. Various models have been proposed from the thin film model (Rutter, 1976; Weyl, 1959) to the island-channel model (Raj & Chyng, 1981). These models have been improved by suggesting dynamic evolution of the grain boundary contacts (Dysthe et al., 2003; Ghoussoub & Leroy, 2001; Lehner & Bataille, 1985) and activating effect of microcracks (den Brok, 1998; Gratier et al., 2009; Gratier et al., 2014; Gratz, 1991).

Another crucial characteristic of grain boundary contacts is the difference between grain boundaries where two similar minerals are in contact (like-contact) and grain boundaries where the two minerals in contact are

different (unlike-contact). In the sample studied here, we see clearly this difference in like- and unlike-contacts by the contrasting behavior of the monomineralic rigid objects compared with the behavior of the polymineralic deformed shale around these rigid objects (Figures 6a and 6b). It appears that unlike-contacts in polymineralic rocks are much more efficient for stress-driven mass transfer than like-contacts in monomineralic rocks. This effect is even enhanced in the presence of phyllosilicates, as it has been shown in natural deformation (Bathurst, 1971; Heald, 1955) and confirmed by experiments (Hickman & Evans, 1995; Meyer et al., 2006; Renard et al., 2001; Renard et al., 1997; van Noort et al., 2007). Quantifying to what extent variations in the amount of unlike-contacts may affect the deformation is not easy. However (Zubtsov et al., 2004), showed that the fastest rate of compaction of mixed aggregate of soluble and insoluble grains is obtained with a content of soluble grains in the 45%–75% range, the higher value being here closed to the value of the calcite content in the studied rocks.

A supplementary effect could be seen here, which is related to the characteristics of the sedimentation of the fine-grained rocks of the Bourg d'Oisans basin associated with slow decantation of small particles offshore (Barfety et al., 1972). EBSD with smaller pixel size and SEM-EDS studies show that the rock contains a certain amount of extremely fine particles with grain size well below 0.5  $\mu\text{m}$ . Extremely fine particles are known to interfere with recrystallization (Poirier, 1985) which is not likely to have occurred here: see discussion below on the CPOs in the pole figures (Figures 3d and 3e, 4d and 4e, and 5d and 5e). Furthermore, second-phase pinning at grain boundaries keeps the grain size small by inhibiting grain growth, further promoting deformation by diffusive mass transfer (Herwegh et al., 2011). Moreover, the coating of the grains by a dust of extremely fine particles during the sedimentation certainly influences the behavior of the grain boundaries once the rock is consolidated by promoting numerous bridges of unlike-contacts along grain boundaries even between the same mineral and so facilitating diffusive mass transfer. The difference between like- and unlike-contacts is due to a more efficient self-healing process of the grain boundary when the same minerals are in contact; grain boundary healing reduces the fluid interconnection, which reduces the efficiency of the diffusion along grain boundaries. This self-healing process is driven by the lowering of surface energy (Brantley et al., 1990; Gratier & Jenatton, 1984; Smith & Evans, 1984; van Noort et al., 2008). These self-sealing processes are time dependent and must be even more important in the slow natural deformation compared to the relatively fast deformation that is characteristic of laboratory experiments. Healing processes have the opposite effect of microcrack activation along grain boundaries and the two effects compete in deformation depending on the thermodynamic conditions of the deformation (Gratier et al., 2014). It is therefore likely that the geometry of the grain contacts evolves with time (Gratier, Dysthe, & Renard, 2013; Gratier et al., 2014; Renard et al., 2012; van den Ende et al., 2019; van Noort et al., 2008).

The shapes of the grains are not strictly equant but slightly elongated (Figures 3c, 4c, and 5c), which is a frequent observation in natural rocks. Examples of grain shape analyses in deformed limestones (Ebner et al., 2010) and shales (Saur et al., 2020) and even for manufactured limestone and natural sands (Huang & Wang, 2017) show an asymmetrical normal distribution of the grain shapes, which is of the same type as the distribution measured in the sample analyzed here (Figures 3c, 4c, and 5c). Several explanations of this observation are possible. First, the grains are not necessarily equant during the deposition process. Second, even in tectonically internally “undeformed” rocks, grains have experienced diagenetic pressure solution creep that tends to preferentially dissolve grain boundaries perpendicular to the main vertical compression, as suggested by (Saur et al., 2020). This may be seen by the preferential dissolution of the growth rings of the dolomite grains in Figure 7a. The slight difference of the grain shapes between the two sections along the principal strain axes  $X$ - $Z$  and  $X$ - $Y$  is of the order of 10% of the grain size for quartz and calcite and may be associated with pressure solution deformation at grain scale in parallel with grain boundary sliding. It must be noted that both the acquisition of grain shape preferred orientation and the grain boundary sliding that require mass distribution from high to low stress surfaces may imply replacement processes in which primary mineral dissolution and secondary mineral precipitation are coupled at the mineral interfaces (Putnis & Putnis, 2007). Such dissolution precipitation processes are discussed in more details in other studies (Malvoisin & Baumgartner, 2021; Ruiz-Agudo et al., 2014; Wintsch & Keewook, 2002). The grain deformation could also be related to the slight crystallographic preferred orientation revealed on the pole figures (Figures 3f, 4f, and 5f). However, due to the very weak CPOs in these pole figures and to the lack of relationships between GOS/MOS and grain shape/grain size (Figures 3d and 3e, 4d and 4e, and 5d and 5e) the contribution of dislocation creep may be considered as negligible. One could wonder if dislocation creep has accommodated the sliding between the grains and then grain size may have been reset by recrystallization.

Such a process described in naturally deformed marble (Bestman & Prior, 2003) leaves some evidences of large dislocation creep, which is not the case here. Moreover we compared the grain size characteristics of the highly deformed rocks in the Bourg d'Oisans basin with rocks collected in an area less deformed west away of the Oisans massif with the same age and characteristics of sedimentation (Figures 1h–1j). Results show that the distribution and the characteristics of the grain size is similar in the deformed Bourg d'Oisans formation and in the less deformed rocks, and thus grain size did not change significantly during the development of the deformation (same mode and almost the same mean or median values Figures 1h–1j). Thus, we conclude that the present-day grain size in the highly deformed zones is very close to the initial grain size after sedimentation. So all the observations strongly support that the deformation is accommodated predominantly by pressure solution grain boundary sliding.

When considering possible coupling between shearing friction and pressure solution creep processes (Bos et al., 2000; den Hartog and Spiers, 2014; Niemeijer & Spiers, 2007), it must be noted that in such models the phyllosilicates should be well reoriented parallel to the maximal elongation, with only slight curving around the soluble minerals (e.g., quartz, calcite) and this microstructure is not observed in our sample. Here, the phyllosilicates are less reoriented than the soluble minerals (Figures 3d, 4d, and 5d) and there are numerous observations that indicate that the phyllosilicates that indent the soluble minerals did not rotate (Figure 7a). Moreover, in rate-and-state frictional model (Chen & Spiers, 2016), it is shown that a key requirement for the model to be applied is that a significant amount of porosity must exist in the gouge material or can be created and modified by shear-induced dilation. This model further predicts that as the slip rate decreases to a slower geological deformation rate, the porosity of the shear band approaches zero. Thus, friction-controlled slip at grain boundaries becomes negligible and deformation is controlled by pressure solution. At the slow deformation rate of the very low porosity sediment deformed at 5–8 km depth, it is likely that the contribution of friction is negligible. Conversely, in the basement that is mostly deformed along faults and shear zones (Bellanger et al., 2014), it is likely that friction is a key mechanism of the deformation including strain weakening processes associated with earthquakes and possible strain strengthening postseismic processes in the granular gouges. The transition from transfer-controlled to friction-controlled processes is seen on the field by comparing the relatively homogeneous ductile deformation of the sediment within the basin with the deformation localized along shear zones at all scales in the basement (Figure 1). The crucial difference is linked to the rate of pressure solution, which is strongly dependent on the grain size and on the characteristics of mass transfer along grain boundaries (see discussion of the flow law below).

Finally, grain sliding controlled by pressure solution at grain boundaries in the sedimentary cover must have been difficult at the end of the Alpine deformation peak because some late brittle deformation is also observed. Several large horizontal veins, hundreds of meters long and 10 cm wide (Figure 2c) developed at relatively low temperature of  $150 \pm 3^\circ\text{C}$  indicated by fluid inclusion studies in the quartz and calcite filling of these veins (Jenatton, 1981). These veins imply a mechanism of ductile-brittle deformation coupled to pressure solution and fluid advection (Gratier, Dysthe, & Renard, 2013) that represent only a very small part of the total deformation of the sedimentary cover (less than 0.01%) and that marks the end of the superplastic deformation flow regime. These late ductile-brittle deformation events probably occurred in parallel with the development of a crenulation cleavage (S2 in Figure 1c), also developed at low temperature because the main mobile element is calcite, whereas quartz does not significantly dissolve. This process only happens at low temperatures of the order of 100–150°C (Gratier, Dysthe, & Renard, 2013).

#### 4.2. Flow Laws for Superplastic Creep

A flow law describing large superplastic deformation requires a geometric model of grain evolution. In their diffusion-accommodated model that describes superplastic flow (Ashby & Verral, 1973), used a 2D idealized tessellation of hexagonal grains in which pure shear deformation occurs with a unit step of deformation of four hexagonal grains (Figure 8a). These grains move by sliding along their boundaries, from an initial horizontal to a final vertical lengthened shape. As a result, an elemental elongation is given by the ratio  $3a/2h = 1.73$ ,  $a$  being the length of the hexagons and  $h$  their apothem. For this unit step, these authors give only an intermediate state, which is associated with the transformation of the unit of four grains from horizontal to vertical hexagons. Ashby and Verral (1973) evaluated the mean distance of mass transfer between the zones where volume must be removed and the zones where material are stress-relaxed by the grain sliding. They proposed a value  $0.28d$ , where  $d$  is the

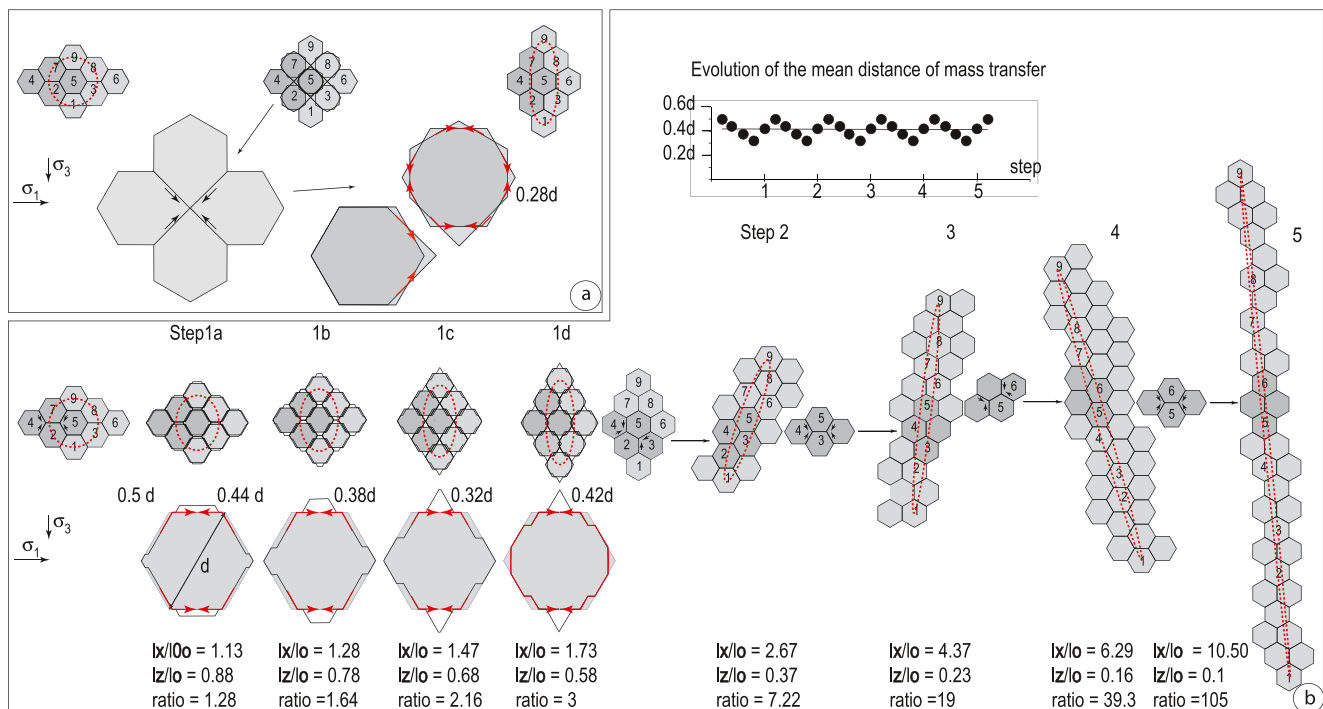


**Figure 8.** Models of stress-driven grain boundary sliding at grain scale that describes superplastic flow behavior. (a) Pressure solution grain sliding within a unit of four grains from horizontal to vertical hexagon (above) leading to horizontal shortening of 0.58 and associated vertical elongation of 1.73 with a unique step of transition in an intermediate state (below) accommodated by mass transfer along solid grain boundary (red arrows) with a mean distance of mass transfer of  $0.28d$ ,  $d$  being the grain size, adapted from (Ashby & Verral, 1973). (b) Pressure solution grain sliding within the same unit of four grains from horizontal to vertical hexagon (above) leading to the same horizontal unit shortening of 0.58 and associated unit vertical elongation of 1.73 (1d), but with progressive incremental change of shape (1a-b-c-d) with mean distance of mass transfer that evolves with time from  $0.5d$  (for the initial state) to  $0.32d$  with mean value of  $0.42d$  (see diagram). With such a model several steps of incremental deformation (here five are represented: 1 to 5) can lead to very large strains: vertical elongation ( $l_x/l_0$ ) above 4 and shortening ( $l_z/l_0$ ) lower than 0.25, as observed in the field. Note that for geometric reasons the deformation of the unit of four grains needs to be oblique at  $30^\circ$  of the elongation for some steps (2 and 4) but may be kept parallel to it for other steps (3 and 5), leading to very large near vertical elongation (10.5) and near horizontal shortening (0.1) (step 5).

grain size (Figure 8a). This is a crucial parameter of their flow law (see below). However, this value is linked to the use of only one intermediate step. We used an alternative model always with the same unit of deformation of four hexagonal grains that move by grain sliding from an initial horizontally to a final vertically lengthened shape, but with a more incremental progressive deformation (Figure 8b). In such a model that we describe here in four increments, a-b-c-d (Figure 8b), the mean distance of mass transfer is evaluated at the beginning and at each increment and seen to evolve with time from  $0.5d$  to  $0.32d$  with a mean value of about  $0.42d$ . This evolution is shown in a diagram describing this evolution with time (Figure 8b).

Moreover, the continuation of the deformation toward an elongation value larger than 1.73 is not described in the model of (Ashby & Verral, 1973). When modeling this evolution for five cumulative step units, so toward more elongation with a final elongation value larger than 10 (step 5, Figure 8b), geometric constraints imply that the direction of the second unit step of sliding of the grains must be oblique at  $30^\circ$  of the direction of sliding of the first unit step (step 2 Figure 8b) leading to a maximal elongation which is not vertical. Then, the third step allows the same direction of sliding as the first step, leading to a total elongation of 4.37 not far from vertical. The fourth step must also occur at  $30^\circ$ , possibly in the other sense with non-vertical elongation and then the fifth step leads to a near vertical large elongation of 10.5 (Figure 8b). So high values of elongation may be modeled by such incremental sliding, as it is observed in the deformed cover of the Oisans massif (Figure 1d3). Of course, this conceptual model is an idealization of the reality. As observed in thin sections, the grains have neither exactly the same size nor the same shape. So deformation must also involve grain rotation and change in shape due to diffusive mass transfer, and the heterogeneous deformation of the grains linked to the difference in size and shape may also control deformation (Ashby & Verral, 1973).

In their proposed diffusion controlled flow law (Ashby & Verral, 1973), considered that mass transfer occurs both by grain boundary diffusion and bulk diffusion within the grains. However, in most cases when applied to

crustal deformation with relatively low temperature, only grain boundary diffusion is considered (Boullier and Guéguen, 1975; Rutter et al., 1994; Schmid et al., 1977) and the flow law is written:

$$\dot{\epsilon} = A 3 D_b w \delta \sigma_d / k T d^3 \quad (1)$$

where  $\dot{\epsilon}$  is the strain rate,  $A$  is a numerical coefficient depending on the geometry of the mass transfer path with a value of about 100 in the model derived by (Ashby & Verral, 1973) due to the low value of the transfer path ( $0.28d$ ),  $d$  is the grain size,  $D_b$  is the solid grain boundary diffusion,  $w$  is a mean effective thickness of the diffusion pathway along grain boundaries,  $\delta$  is the atomic volume of the transported solid,  $\sigma_d$  is the differential stress,  $kT$  is the Boltzmann's constant times the absolute temperature. Extrapolation of laboratory data to geological strain rates in a temperature range of 400–600°C show that grain boundary sliding is predicted for small grains of less than 10  $\mu\text{m}$  diameter under a low stress of 0.1 MPa (Schmid et al., 1977). However, the temperature is much lower in our case study, in the range 200–335°C. In these conditions the role of pressure solution creep in the ductile deformation must be considered (Gratier, Dysthe, & Renard, 2013). Pressure solution is an en-series process implying successive steps of dissolution, diffusion, and reprecipitation. If one of these steps is much slower than the other ones, it controls the strain-rate. Consequently, several creep laws are possible depending of the rate limiting step (Lehner, 1990, 1995; Pluymakers & Spiers, 2014; Raj, 1982). In these creep laws the relationship between strain rate and some parameters are different allowing to distinguish them. For the mobile minerals (mainly calcite and quartz), in the conditions of pressure and temperature examined in this study and with the low-porosity compacted structure of the rocks, diffusion is the more likely limiting step (see review of experimental work in (Gratier, Dysthe, & Renard, 2013)). However, in such conditions, some experiments on calcite show possible reaction control in case of inhibition of interfacial reactions by the presence of phosphate or  $\text{Mg}^{2+}$  in the intergranular fluid (Zhang & Spiers, 2005; Zhang et al., 2011). In the studied deformation of the Oisans massif the only parameter that can be tested is the grain size effect ( $d$ ), which is inversely proportional to strain-rate either as  $1/d$  for reaction control or  $1/d^3$  for diffusion control. Observations show that large strain values associated with ductile deformation are limited to very fine-grained rocks with a significant number of unlike contacts. Conversely, the ductile deformation of nearby coarse-grained rocks, also with a significant fraction of unlike contacts, such as in calcareous dolomites in the Trias and granitoids in the basement, is almost negligible (Bellanger et al., 2014; Dumont et al., 2008). This crucial effect of the grain size supports a diffusion-controlled pressure solution creep law. When using such type of diffusion controlled pressure solution grain sliding flow law, the flow law derived from pressure solution indenter experiments is (Dewers & Ortoleva, 1990; Gratier et al., 2009; Rutter, 1976):

$$\dot{\epsilon} = A D w c V_s \left( e^{\frac{3V_s \sigma_d}{RT}} - 1 \right) / d^3 \quad (2)$$

with the same parameters as above, plus  $c$  ( $\text{mol. m}^{-3}$ ) being the solubility of the diffusing solid into a thin grain boundary fluid phase,  $V_s$  ( $\text{m}^3 \text{mol}^{-1}$ ) is the molar volume of the stressed solid,  $R$  ( $8.31 \text{ J mol}^{-1} \text{ K}^{-1}$ ) is the gas constant,  $T$  ( $^\circ\text{K}$ ) is the temperature,  $D$  ( $\text{m}^2 \text{ s}^{-1}$ ) is the diffusion constant along the trapped fluid phase at the stressed interface,  $w$  (m) is the mean thickness of the fluid interface along which diffusion occurs,  $\sigma_d$  (Pa) is the differential stress between zones of dissolution and zones of redeposition (Figure 8) corresponding to the difference between normal stress on a dissolution surface and fluid pressure in the zone of redeposition in indenting experiments, and  $d$  (m) is the grain size.

In order to test the effect of the various parameters we built deformations maps (Figure 9) with a large range of strain rate and stress values plotted relative to the grain size instead of temperature, as is commonly done for deformation maps because pressure solution creep is more sensitive to grain size than to temperature (Elliott, 1973). We create these maps for two types of temperature and depth conditions, corresponding to minimum and maximum values recorded by the study of fluid inclusions in redeposited minerals during the deformation process linked to a 40°C/km temperature gradient: 200°C (5 km depth), and 320°C (8 km depth). These deformation maps are constructed both for quartz and calcite. We used the values of solubility and molar volume given in the literature (Sharp & Kennedy, 1965; Weill & Fyfe, 1964). For the value of the numerical coefficient  $A$ , following the modeling of incremental deformation grain sliding (Figure 8b) with mean distance of mass transfer of  $0.42d$  very close to the value for Coble creep ( $0.43d$ ), we use the same value of  $A = 14$  as in the eponym creep law. This value of  $A$  is nearly one order of magnitude lower than the value used by (Ashby & Verral, 1973), who considered a lower distance of mass transfer ( $0.28d$ ). This choice is discussed below. Finally, the parameter for which there

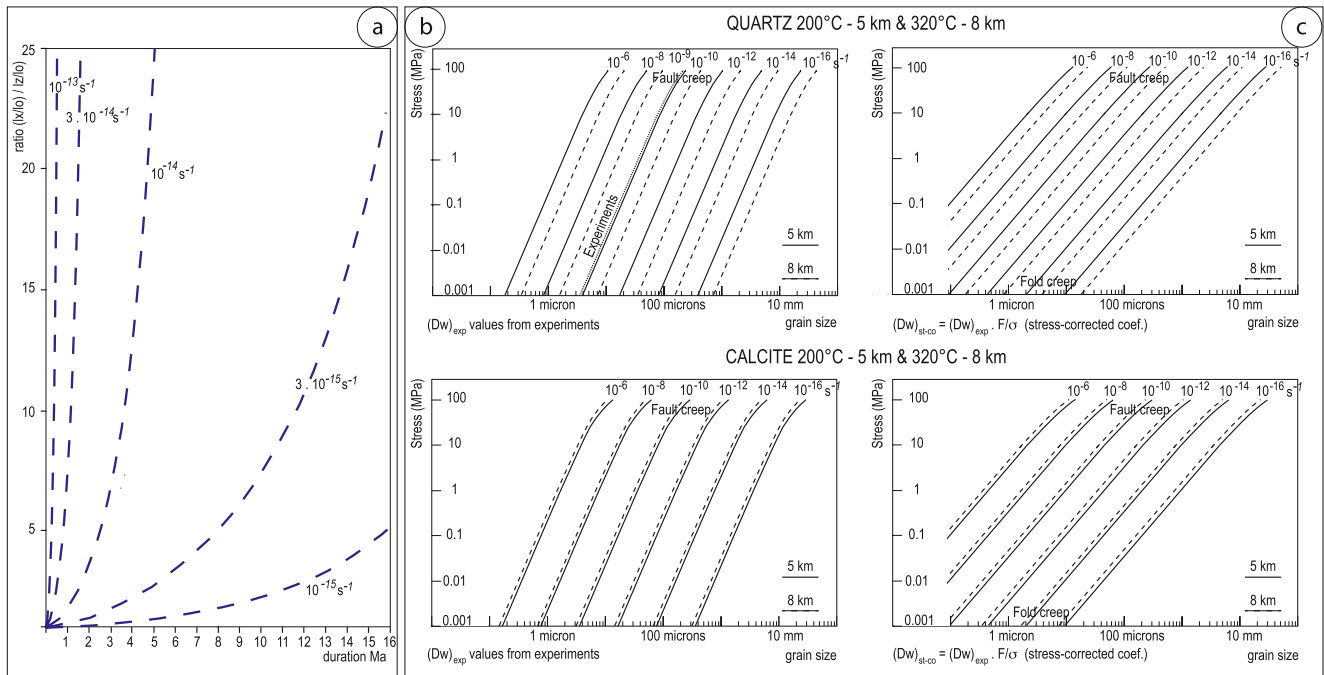


**Figure 9.** Pressure solution grain boundary sliding as mechanism of large superplastic deformation in the upper crust. (a) Relationship between incremental strain rate in large finite deformation and durations for pure shear deformation, adapted from (Pfiffner & Ramsay, 1982). (b) Deformation maps in a differential stress versus grain size plot, for quartz (top) and calcite (bottom) at two different depths: 200°C–5 km (continuous lines) and 320°C–8 km (dashed lines) corresponding to the observed conditions of the deformation at strain rates ranging from  $10^{-6}$  to  $10^{-16} \text{ s}^{-1}$  using the mass transfer characteristics product  $Dw = 6 \cdot 10^{-19} \text{ m}^3 \text{ s}^{-1}$  at 350°C (mean diffusion coefficient within fluid phase trapped along grain boundary ( $D$ ) times mean thickness of this trapped fluid phase along grain boundary ( $w$ )), deduced from pressure solution experiments on quartz (Gratier et al., 2009), the dotted line at strain rate of  $10^{-9} \text{ s}^{-1}$  is the best approximation of this experiment. The slight change of slope of the strain rate lines expresses the effect of the exponential relation with differential stress that becomes negligible below about 10 MPa. (c) Same type of deformation maps but with the use of a stress-corrected slowness coefficient  $F/\sigma_d$  for the  $Dw$  parameter where  $F$  is a micro-cracking yield strength (taken at a conservative value of 100 MPa), and  $\sigma_d$  is the driving stress. On the deformation maps, we report the approximate conditions of some examples of pressure solution creep observed in active fault creep (150–200°C, 60 MPa, 100 microns grain size) (Gratier et al., 2011), and in natural deformation in fold creep zone (200–335°C, 0.001 MPa, 1–5 microns grain size, this work).

is the largest uncertainty, probably of several orders of magnitude, is the product  $Dw$  that characterizes the diffusivity along the path of transfer (diffusion coefficient times width of a mean trapped fluid phase along the grain boundary).  $Dw$  values are found to range from  $10^{-17}$  to  $10^{-19} \text{ m}^3 \text{ s}^{-1}$  from experiments on several minerals and under various deformation conditions (Dysthe et al., 2002; Gratier et al., 2009; van Noort et al., 2007; van Noort et al., 2011; Zhang et al., 2010). We used here the value of  $6 \cdot 10^{-19} \text{ m}^3 \text{ s}^{-1}$  obtained in experiments of pressure solution on quartz at 350°C (Gratier et al., 2009), very closed to the value of about  $10^{-19} \text{ m}^3 \text{ s}^{-1}$  obtained for calcite at 150°C (Zhang et al., 2010).

Deformation maps using this experimental value are shown in Figure 9b. One can note that there is only a slight difference between quartz and calcite: in this range of pressure and temperature conditions, the mobility of these two minerals is observed to be almost the same (Figure 6). Simply, the evolution with depth for these two minerals is opposite: mobility under stress increases with depth for quartz and slightly decreases for calcite due to their opposite evolution of solubility with temperature (Gratier, Dysthe, & Renard, 2013).

### 4.3. Knowledge of and Uncertainties on the Parameters of Superplastic Flow Laws in Nature

When attempting to extend the deformation maps deduced from experiments (Figure 9b) to natural deformation, one must first compare the effect of the various parameters of the flow law in experiments and in natural deformation.

For the differential stress values, several observations indicate that in the studied natural deformation the values must be low. First, the minimum intersection angle of  $30^\circ$  between the two successive slaty and crenulation cleavages (Figure 1c) (Gratier & Vialon, 1980) means that dissolution could occur on planes that are oblique to

the maximum compressive stress without slipping. When using experimental data on anisotropic rocks, one finds maximum values in such a case of less than 10–25 MPa (Gratier, Dysthe, & Renard, 2013). Another observation is that some slaty cleavage planes are filled with crystallizations even in the hinge of folds (Figure 2d). These crystallizations are boudinaged and are as vertically elongated as the deformed rock. It has been suggested that this structure could result from episodic events of hydraulic fracturing and sealing during the development of cleavage (Gratier, Dysthe, & Renard, 2013). Opening a fracture by increasing fluid pressure involves overcoming the tensile strength plus the stress perpendicular to the fracture. In case of anisotropic rocks, opening cleavage planes implies differential stress lower than the difference between the tensile strength parallel and perpendicular to the cleavage, so lower than 10 MPa (Gholami & Rasouli, 2014). Moreover, the level of stress is imposed by the rate of loading at the boundary of the deformed zone and by the creeping characteristics of the rock; consequently the differential stress could be very low if the conditions of deformation are favorable. In actively deforming zones, the mean stress drop associated with upper-crustal earthquakes is about 10 MPa with values ranging from more than 100 MPa to less than 1 MPa (Cocco et al., 2016). For example, in the Himalayas, some earthquakes are associated with a very low stress drop below 1 MPa (Sharma & Wason, 1994). Consequently, in such a case, neighboring ductile process spread over a larger volume may be associated with stress levels much lower than 1 MPa.

For the strain rate, assuming steady state flow, steady strain rate is associated with an exponential relation between the value of the finite strain and the duration of the deformation (Pfiffner & Ramsay, 1982) (Figure 9a). Steady strain rate of  $10^{-14} \text{ s}^{-1}$  is needed in order for the observed strain ratio of 4–16 to develop in pure shear deformation within 2.5–4.5 Ma. Strain rate of  $10^{-13} \text{ s}^{-1}$  would reach such high strain values within less than 0.5 Ma. More than 16 Ma would be required to reach such high strain values at a strain rate of  $3 \cdot 10^{-15} \text{ s}^{-1}$ . The strain rate may be faster if deformation is not continuous and occurs in bursts. If for example, seismic deformation of the basement controls the strain rate of the pinched sedimentary basins, one may consider that deformation episodes are only transient, such as postseismic deformation, and so in this case occur at larger strain rates than expected. However, in this case one must see the associated fracturing of the grain that are associated with the seismic events as seen in active faults (Gratier et al., 2011) that is not seen here. Moreover, when relatively high strain rates, of the order of magnitude of  $10^{-10} \text{ s}^{-1}$ , are observed in active continental strike slip faults, they are always associated with a much lower width of the deformation zones, on the order of some meters for the creeping zone of the San Andreas fault (Zoback et al., 2010) and so with more localized deformation than the 10 km wide basin considered in this study. Consequently, the uncertainty on the strain rate is probably less than one order of magnitude around  $10^{-14} \text{ s}^{-1}$ .

For the grain sizes, when using the experimental data the deformation maps of Figure 9b show that for low stress values of 0.001 MPa, grain sizes of 70–200 microns could accommodate a strain rate of  $10^{-14} \text{ s}^{-1}$  for both calcite and quartz. With stress values of 0.01 MPa grain size could be about 150–350 microns. There are a number of other polymineralic rocks in the surrounding areas of the Bourg d'Oisans basin with a range of grain sizes of several hundred micrometers, such as Triassic calcareous dolomite and Hercynian granite, gneiss migmatite (Barfety et al., 1972), and none show significant internal ductile deformation developed during alpine deformation (Dumont et al., 2008), attesting of the inefficiency of pressure solution creep for such large grain sizes. Conversely, these rocks show evidence of brittle deformation and fracturing associated with alpine deformation as thrusts and cataclastic reverse shear zones that accommodate the shortening of the basement (Bellanger et al., 2014) (Figure 1c). So the deformation maps of Figure 9b show that when using experimental data the potential efficient grain size is much larger, of a few orders of magnitude, than the one observed in natural deformation associated with folding and cleavage development, which ranges from 1 to 5 microns, depending on which parameters we choose (mode, mean or median values, see Figures 3–5). These deformation maps are compatible with observations of pressure solution creep in active fault zones where relatively high strain rates of about  $10^{-10} \text{ s}^{-1}$  at relatively large stress values (60 MPa) are associated with grains of relatively large size of several hundred micrometers (Gratier et al., 2011). However, it must be noted that, in this case, pressure solution creep is enhanced by fracturing of the grains. This process of fracturing of the grains mostly develops during earthquakes, and reduces the distance of mass transfer, enhancing pressure solution creep. Moreover, because the fractures may heal progressively, such enhancement of creep is a transitory post-seismic process (Gratier et al., 2009; Renard et al., 2000). It is not the case in the studied example where evidence of grain fracturing is very rare. Moreover, as discussed above the strain rate of the observed deformed rock is estimated to be about  $10^{-14} \text{ s}^{-1}$  with an uncertainty of about one order magnitude. Consequently if we compare the strain rate of  $10^{-9}$

$s^{-1}$  from experiments in Figure 9b that could theoretically be associated with deformation of fine grains aggregate of 1–5 microns with the strain rate of the studied natural deformation of  $10^{-14} s^{-1}$  that is really associated with the same range of grain size from 1 to 5 microns, there is a discrepancy factor of  $10^5$ . What other parameters of the pressure solution creep law may be overestimated by such a large value?

The  $A$  parameter of 100 used in the (Ashby & Verral, 1973) model contributes even more to the efficiency of the creep law so we can keep the used value of 14. The distance of mass transfer could be larger than modeled (Figure 8). However, it is difficult to imagine mass transfer distances much larger than the grain size, for geometrical compatibility reasons and by the observation that the size and distribution characteristics of the grains remain constant with the increase of strain (Figures 1h–1j).

So the last and only parameter that can be significantly modified to best fit the data is the product of the parameters  $D$  and  $w$  that characterizes the mass transfer rate. Due to the large uncertainty on the characterization of fluid phase trapped under stress along grain boundaries, researchers often use the combined mass transfer parameter  $Dw$  in creep laws. This parameter expresses the product of the mean diffusion coefficient ( $D$ ) along grain boundaries and the mean width of the path transfer ( $w$ ), corresponding to the mean thickness of the fluid phase trapped at grain boundaries. When evaluated from experiments, the product  $Dw$  ranges from  $10^{-17}$  to  $10^{-19} m^3 s^{-1}$  (Dysthe et al., 2002; Gratier et al., 2009; van Noort et al., 2007; van Noort et al., 2011). In Figure 9b we used the value of the  $Dw$  parameter  $6 \cdot 10^{-19} m^3 s^{-1}$  that has been measured by long duration quartz indenting experiments in laboratory at  $350^\circ C$  (Gratier et al., 2009), very closed to the value obtained by compaction creep of wet granular calcite at  $150^\circ C$  (Zhang et al., 2010). The conditions of the deformation correspond to natural quartz deformation at strain rate of  $10^{-9} s^{-1}$ , with differential stress of 100 MPa and grain size of 200 microns (Gratier et al., 2009). The problem is that we know (see discussion above) that the natural deformation occurs at much slower rate, around  $10^{-14} s^{-1}$ , leading to a possible decrease of the  $Dw$  factor of  $10^{-5}$ . What could explain such a difference?

The effect of stress on this mass transfer parameter is complex. It has been shown from experiments and modeling that increasing stress could reduce the width of the mass transfer path ( $w$ ), and consequently decreases the rate of mass transfer (de-Meer et al., 2002; Dysthe et al., 2002; van Noort et al., 2007). However, another effect of increasing stress is its activation effect associated with the development of microcracks at the grain boundary scale (den Brok, 1998; Gratier et al., 2009; Gratier et al., 2014; Gratz, 1991). In such a case the grain boundary structure is considered as an island-channel network (Raj & Chyung, 1981) with island being like- or unlike-contacts possibly including fluid phase trapped under stress. Network of channels are clearly seen (Dysthe et al., 2003; Gratier et al., 2009) that can reduce to isolated fluid inclusions rooted on dislocations (Gratier et al., 2005; Schenk et al., 2005). When observed after the experiments these microcracks are sealed as they are sealed in nature and so very difficult to reveal at the required nanoscale. However, it is likely that they correspond to corrosion cracks that develop continuously during the loading under relatively high stresses (Anderson & Grew, 1977; Rostom et al., 2013). Consequently, there is likely a competition between two opposite effects. On the one hand, open cracks during their subcritical propagation enhance mass transfer along grains boundary because diffusion in the free fluid that filled the crack is much faster than the diffusion in the solid bridge between the cloud of fluid inclusions or more generally along any fluid phase trapped under stress. On the other hand, a slowing down effect is due to microcrack healing that drastically reduces the diffusion along the micro-cracked grain boundaries. This effect is time dependent as is more generally grain boundary healing. Like-contacts evolve with time toward a cloud of fluid inclusions consequently reducing diffusion that must occur along the solid bridges between the inclusions (van Noort et al., 2008). In case of unlike-contacts the surface energy is lowered for each mineral boundary also reducing the path for diffusive mass transfer with time (Gratier et al., 2014). Therefore, the overall rate of deformation is controlled by a competition between activating (cracking) and slowing down (healing) effects. In experiments always conducted under relatively high stress and fast strain rate, the cracking effect may dominate. When reducing stress and strain rate values, this activating effect of subcritical cracks may progressively disappear.

#### 4.4. A Flow Law for Superplastic Creep in Fine-Grained Naturally Deformed Rocks

To take into account the effect of microcracking at grain boundaries that dominate in experiments and disappear in natural deformation, we introduce a stress-corrected slowness coefficient associated with the parameter  $Dw$  deduced from experiments. This slowness coefficient is used to express the fact that when the stress is lower than a microcracking yield stress, the mass transfer efficiency may be reduced. Stress is certainly not the only

factor that is responsible for crack development, the density of flaws in the mineral is also important. This is why pressure solution experiments conducted at relatively high stress lead to strain rate values that are largely dispersed (Croizé et al., 2010; Gratier et al., 2009). However, due to the lack of constraints, we simply choose a linear decrease as the ratio of a microcracking yield stress over the loading stress to build alternative deformation maps. It must be noted that the stress value is linked to the strain rate (or more precisely to the rate of loading) so this slowness factor could have been incorporated into the strain rate when comparing experimental to geological behavior. But for the explored deformation conditions, strain rate and stress parameters are linked by a nearly linear relation at least below stress values of about 10 MPa, where the effect of the exponential relation becomes negligible (Figures 9b and 9c). So an alternative flow law is proposed as follows:

$$\dot{\epsilon} = 14 (D w)_{st-co} c V_s (e^{\frac{3V_s \sigma_d}{RT}} - 1) / d^3 \quad (3)$$

where the parameters are the same as in Equation 2, and  $(D w)_{st-co} = (D w)_{exp} F / \sigma_d$  where  $(D w)_{st-co}$  and  $(D w)_{exp}$  are the diffusion coefficient times the mean width of the boundary path of transfer.  $(D w)_{exp}$  is the value obtained from experiments under relatively high stress (more than 100 MPa) and relatively fast strain rate (about  $10^{-9} \text{ s}^{-1}$ ) (Gratier et al., 2009).  $(D w)_{st-co}$  is the stress-corrected value by the factor  $F / \sigma_d$ ,  $F$  being a microcracking yield stress (taken here as a conservative value of 100 MPa), and  $\sigma_d$  the driving differential stress.

Adding this slowness parameter leads to new deformation maps (Figure 9c) that show the same pattern for the highest stress values but that correspond much better to the microstructures observed in the Oisans deformed basins, for both calcite and quartz, where low strain rates of  $10^{-14} \text{ s}^{-1}$ , low stress values (0.001 MPa) are inferred, associated with the observed small grain sizes (1–5 microns) for what is called “folding creep” in Figure 9c. This possible evolution of the characteristics of mass transfer depending on stress and strain rate would need to be investigated in other locations where fine-grained sedimentary or volcanic rocks have been highly deformed under upper crustal conditions, especially at various stress levels in active fold and fault creeping zones. Pressure solution grain boundary sliding represents a very efficient mechanism of ductile deformation of fine-grained polymineralic rocks. As a viscous creep mechanism it may be a key mechanism for example, in the numerical modeling of the interplay between seismic and aseismic deformation in the Earth's upper crust (Beall et al., 2022).

## 5. Conclusion

Large superplastic deformation is observed in fine-grained calcareous shales transformed to slate schists of the Oisans massif in the Western Alps, deformed at temperatures in the range 200–335°C and depths in the range 5–8 km, with little to no evidence of brittle deformation. EBSD analyses on two perpendicular thin sections parallel to the principal strain directions show that the low shape ratios of the grains (1.4–1.6) do not match the actual finite strain values recorded by the markers of the outcrop-scale deformation (truncated belemnites, folded veins), neither in the plane of maximum elongation and maximum shortening (with shape ratio of 6.7) nor in the plane of maximum elongation and minimum shortening (with shape ratio of 2.4). Consequently, a grain boundary sliding mechanism is required in order to explain the measured large finite strain values.

The slightly elongated shape of the grains may be related to initial deposition, diagenetic evolution, or tectonic deformation by pressure solution creep. Evidence of local intergranular pressure solution mass transfer are observed around rigid objects, such as pieces of veins or fossils, with stress-driven dissolution of the most soluble minerals (e.g., quartz, calcite, dolomite, albite) and passive concentration of the least mobile minerals (e.g., muscovite, chlorite and Fe-Ti oxides) in the zone of maximum stress. Mixed together, the most soluble minerals, which represent about 95% of the rock volume, accommodate the deformation by pressure solution grain boundary sliding, whereas the least soluble minerals are partially reoriented. Very locally, some clusters of soluble minerals, which have been healed together in veins or fossils, are much more resistant to the pressure solution process and act as rigid objects.

Starting from an idealized tessellation of hexagonal grains, we propose geometric models of incremental deformation that allow constraining the mean distance of mass transfer which is required to accommodate grain boundary sliding (from 0.28 to 0.42 times the grain size). Using creep laws developed from pressure solution experiments, we build deformation maps for superplastic deformation of fine-grained sediments. Using these deformation maps, we discuss the values of the main parameters of the deformation (pressure and temperature conditions, strain rate, stress, mass transfer characteristics, and geometry of transfer pathway). Our model shows

that diffusion-accommodated superplastic deformation controlled by pressure solution grain boundary sliding may develop under low strain rate ( $10^{-14} \text{ s}^{-1}$ ), and very low differential stress values (0.001 MPa). An important parameter of the flow law is the mass transfer at the grain scale, which is described by the product of the diffusion coefficient times the mean width of the path of diffusion transfer along the grain boundary. This product in the crust is probably several magnitudes lower than the value deduced from pressure solution experiments. We interpret this difference by the development of subcritical microcracks in experiments that may accelerate mass transfer, whereas this effect may disappear at low stress and low strain rate that occur during natural deformation associated with folding and slaty cleavage development.

To conclude, the mechanism of pressure solution grain boundary sliding that we identified in fine-grained slate schists of the Oisans massif in the Western Alps represents an efficient mechanism of large ductile deformation for fine-grained rocks in the upper crust. Indeed, brittle deformation processes are often considered as dominating in the upper crust but observations of seismic—aseismic deformation interplay call for new modeling developments including large strain ductile deformation in the upper crust.

### Data Availability Statement

The EBSD and SEM data are available on the NIRD Research Data Archive <https://doi.org/10.11582/2022.00059>.

### References

- Anderson, O. L., & Grew, P. C. (1977). Stress corrosion theory of crack propagation with application to geophysics. *Review of Geophysics*, *15*(1), 77–104.
- Ashby, M. F., & Verrall, R. A. (1973). Diffusion-accommodated flow and superplasticity. *Acta Metallurgica*, *21*, 149–169.
- Badoux, H. (1963). Les bélemnites tronçonnées de Leytron (Valais). *Bulletin du laboratoire de géologie minéralogie géophysique Musée Géologie Université de Lausanne*, *138*, 1–7.
- Barfety, J. C., Bordet, P., Bornuat, M., Buffiere, M., Carme, F., Debelmas, J., et al. (1972). Vizille 1/50.000 geological map.
- Bathurst, R. G. C. (1971). *Carbonate sediments and their diagenesis* (p. 620). Elsevier.
- Beall, A., van den Ende, M. P. A., Ampuero, J. P., Capitanio, F. A., & Fagereng, A. (2022). Linking earthquake magnitude-frequency statistics and stress in visco-frictional fault zone models. *Geophysical Research Letters*, *49*, e2022GL099247.
- Behrmann, J. H., & Mainprice, D. (1987). Deformation mechanisms in a high-temperature quartz-feldspar mylonite: Evidence for superplasticity flow in the lower continental crust. *Tectonophysics*, *140*, 297–305.
- Bellanger, M., Augier, R., Bellahsen, N., Jolivet, L., Monié, P., Baudin, T., & Beyssac, O. (2015). Shortening of the European Dauphinois margin (Oisans Massif, Western Alps): New insights from RSCM maximum temperature estimates and  $40\text{Ar}/39\text{Ar}$  in situ dating. *Journal of Geodynamics*, *83*, 37–64. <https://doi.org/10.1016/j.jog.2014.09.004>
- Bellanger, M., Bellahsen, N., Jolivet, L., Baudin, T., Augier, R., & Boutoux, A. (2014). Basement shear zones development and shortening kinematics in the Ecrins Massif, Western Alps. *Tectonics*, *33*, 84–111. <https://doi.org/10.1002/2013TC003294>
- Bernard, D., Gratier, J. P., & Pêcher, A. (1977). Application de la microthermométrie des inclusions fluides des cristaux synkinématiques à un problème tectonique. *Comptes Rendus Sommaires de la Société géologique de France*, *5*, 284–288.
- Bestman, M., & Prior, D. J. (2003). Intragranular dynamic recrystallization in naturally deformed calcite marble: Diffusion accommodated grain boundary sliding as a result of subgrain rotations recrystallization. *Journal of Structural Geology*, *25*, 1597–1613.
- Bos, B., Peach, C. J., & Spiers, C. J. (2000). Frictional-viscous flow of simulated fault gouge caused by the combined effects of phyllosilicates and pressure solution. *Tectonophysics*, *327*, 173–194.
- Boullier, A. M., & Guéguen, Y. (1975). S.P. Mylonites: Origin of some mylonites by superplastic flow. *Contributions to Mineralogy and Petrology*, *50*, 93–104.
- Brantley, S. L., Evans, B., Hickman, S. H., & Crerar, D. A. (1990). Healing of microcracks in quartz: Implications for fluid flow. *Geology*, *18*, 136–139.
- Chen, J., & Spiers, C. J. (2016). Rate and state frictional and healing behavior of carbonate fault gouge explained using microphysical model. *Journal of Geophysical Research*, *121*, 8642–8665.
- Cocco, M., Tinti, E., & Cirella, A. (2016). On the scale dependence of earthquake stress drop. *Journal of Seismology*, *20*, 1151–1170.
- Croizé, D., Renard, F., Bjørlykke, K., & Dysthe, D. K. (2010). Experimental calcite dissolution under stress: Evolution of grain contact microstructure during pressure solution creep. *Journal of Geophysical Research*, *115*, B09207.
- Crouzet, C., Ménard, G., & Rochette, P. (2001). Cooling history of the Dauphinoise zone (Western Alps, France) deduced from the thermopaleomagnetic record: Geodynamic implications. *Tectonophysics*, *340*, 79–93.
- de-Meer, S., Spiers, C. J., Peach, C. J., & Watanabe, T. (2002). Diffusive properties of fluid-filled grain boundaries measured electrically during active pressure solution. *Earth and Planetary Science Letters*, *200*(1–2), 147–157.
- den Brok, S. W. J. (1998). Effect of microcracking on pressure-solution strain rate: The Gratz grain boundary model. *Geology*, *26*, 915–918.
- den Hartog, S. A. M., & Spiers, C. J. (2014). A microphysical model for fault gouge friction applied to subduction megathrusts. *Journal of Geophysical Research*, *119*(2), 1510–1529.
- Dewers, T., & Ortoleva, P. (1990). A coupled reaction/transport/mechanical model for intergranular pressure solution stylolites, and differential compaction and cementation in clean sandstones. *Geochimica et Cosmochimica Acta*, *54*, 1609–1625.
- Dumont, T., Champagnac, J. D., Crouzet, C., & Rochat, P. (2008). Multistage shortening in the Dauphiné zone (French Alps): The record of Alpine collision and implication for pre-Alpine restoration. *Swiss Journal of Geosciences*, *101*(1), 89–110.
- Dysthe, D. K., Podladchikov, Y., Renard, F., Feder, J., & Jamtveit, B. (2002). Universal scaling in transient creep. *Physical Review Letters*, *89*(24), 246102.

### Acknowledgments

The authors acknowledge F. Barou, C. Nevado, A. Tommasi at the EBSD platform of the Université de Montpellier, S. Simonsen at the SEM platform of the Goldschmidt Laboratory (Department of Geosciences, University of Oslo), J. McBeck for the suggestion of significant improvements, M. Gidon for his advice on stratigraphic features, M. Sechier for providing Côte Belle basin photographs, and the associate editor B. Almqvist and an anonymous reviewer for their thoughtful reviews. F. R. acknowledges funding from the European Research Council (ERC) under the European Union's Horizon 2020 research and innovation program (Grant agreement 101019628 BREAK). The Research Council of Norway is acknowledged for support to the Goldschmidt Laboratory national infrastructure (project 295894).

- Dysthe, D. K., Renard, F., Feder, J., Jamtveit, B., Meakin, P., & Jossang, T. (2003). High-resolution measurements of pressure solution creep. *Physical Review*, *6801*(1), 317–329.
- Ebner, M., Piazzolo, S., Renard, F., & Koehn, D. (2010). Stylolite interfaces and surrounding matrix material: Nature and role of heterogeneities in roughness and microstructural development. *Journal of Structural Geology*, *32*, 1070–1084.
- Elliott, D. (1973). Diffusion flow laws in metamorphic rocks. *Geological Society of America Bulletin*, *84*, 2645–2664.
- Ford, J. M., & Wheeler, J. (2004). Modelling interface diffusion creep in two-phase materials. *Acta Materialia*, *52*, 2365–2376.
- Gholami, R., & Rasouli, V. (2014). Brazilian tensile strength tests on some anisotropic rocks. *Rock Mechanics and Rock Engineering*, *47*, 1763–1773.
- Ghousoub, J., & Leroy, Y. (2001). Solid-fluid phase transformation within grain boundaries during compaction by pressure solution. *Journal of the Mechanics and Physics of Solids*, *49*(10), 2385–2430.
- Gidon, M. (1998). GEOL-ALP. Retrieved from <http://www.geol-alp.com>
- Gratier, J. P., Dysthe, D. K., & Renard, F. (2013). The role of pressure solution creep in the ductility of the earth's upper crust. *Advances in Geophysics*, *54*, 47–180.
- Gratier, J. P., Guiguet, R., Renard, F., Jenatton, L., & Bernard, D. (2009). A pressure solution creep law for quartz from indentation experiments. *Journal of Geophysical Research*, *114*, B03403. <https://doi.org/10.1029/2008JB005652>
- Gratier, J. P., & Jenatton, L. (1984). Deformation by solution - deposition and reequilibration of fluid inclusions in crystals depending on temperature, internal pressure and stress. *Journal of Structural Geology*, *5*, 329–339.
- Gratier, J. P., Muquet, L., Hassani, R., & Renard, F. (2005). Experimental microstylolites in quartz and modeled application to natural stylolitic structures. *Journal of Structural Geology*, *27*, 89–100.
- Gratier, J. P., Renard, F., & Vial, B. (2014). Postseismic pressure solution creep: Evidence and time-dependent change from dynamic indenting experiments. *Journal of Geophysical Research*, *119*, 2764–2779. <https://doi.org/10.1002/2013JB010768>
- Gratier, J. P., Richard, J., Renard, F., Mittempergher, S., Doan, M. L., Di Toro, G., et al. (2011). Aseismic sliding of active faults by pressure solution creep: Evidence from the San Andreas fault observatory at depth. *Geology*, *39*(12), 1131–1134.
- Gratier, J. P., Thouvenot, F., Jenatton, L., Tourette, A., Doan, M. L., & Renard, F. (2013). Geological control of the partitioning between seismic and aseismic sliding behaviours in active faults: Evidence from the Western Alps, France. *Tectonophysics*, *600*, 226–242.
- Gratier, J. P., & Vialon, P. (1980). Deformation pattern in a heterogeneous material: Folded and cleaved sedimentary cover immediately overlying a crystalline basement (Oisans, French Alps). *Tectonophysics*, *65*, 151–180.
- Gratz, A. J. (1991). Solution-transfer compaction of quartzites: Progress toward a rate law. *Geology*, *19*, 901–904.
- Heald, M. T. (1955). Stylolites in sandstones. *The Journal of Geology*, *63*, 101–114.
- Herwegh, M., Linckens, J., Ebert, A., Berger, A., & Brodhag, S. H. (2011). The role of second phases for controlling microstructural evolution in polymineralic rocks: A review. *Journal of Structural Geology*, *33*(12), 1728–1750.
- Hickman, S. H., & Evans, B. (1995). Kinetics of pressure solution at halite-silica interfaces and intergranular clay films. *Journal of Geophysical Research*, *100*(B7), 13113–13132.
- Hielscher, R., Kilian, R., Mainprice, D., Morales, L. F. G., Bachmann, F., Sorensen, B. E. et al. (2022). MTEX, matlab toolbox for analyzing and modeling crystallographic textures by means of EBSD or pole figure data <https://mtext-toolbox.github.io/index>
- Hiraga, T., Miyazaki, T., Tasaka, M., & Yoshida, H. (2010). Mantle superplasticity and its self-made demise. *Nature*, *468*, 1091–1094.
- Huang, Y., & Wang, L. (2017). Effect of particle shape of limestone manufactured sand and natural sand on concrete. *Procedia Engineering*, *210*, 87–92.
- Jenatton, L. (1981). *Microthermométrie des inclusions fluides des cristaux associés à l'ouverture de fentes alpines: Approche de l'évolution des conditions de pression et de température lors de la déformation* (p. 147). PhD, University Joseph Fourier.
- Kamb, W. B. (1959). Theory of preferred crystal orientation developed by crystallization under stress. *The Journal of Geology*, *67*(2), 153–170.
- Lehner, F. (1990). Thermodynamics of rock deformation by pressure solution. In P. G. M. D. J. Barber (Ed.), *Deformation processes in minerals, ceramics and rocks* (pp. 296–333). Unwim Hyman.
- Lehner, F. (1995). A model for intergranular pressure solution in open systems. *Tectonophysics*, *245*, 153–170.
- Lehner, F., & Bataille, J. (1985). Nonequilibrium thermodynamics of pressure solution. *Pure and Applied Geophysics*, *122*, 53–85. <https://doi.org/10.1007/BF00879649>
- Malvoisin, B., & Baumgartner, L. P. (2021). Mineral dissolution and precipitation under stress: Model formulation and application to metamorphic reactions. *Geochemistry, Geophysics, Geosystems*, *22*(5), e2021GC009633. <https://doi.org/10.1029/2021GC009633>
- Meyer, E. E., Greene, G. W., Alcantar, N. A., Israelachvili, J. N., & Boles, J. R. (2006). Experimental investigation of the dissolution of quartz by a muscovite mica surface: Implications for pressure solution. *Journal of Geophysical Research*, *111*. <https://doi.org/10.1029/2005JB004010>
- Niemeijer, A. R., & Spiers, C. J. (2007). A microphysical model for strong velocity weakening in phyllosilicate-bearing fault gouges. *Journal of Geophysical Research*, *112*, B10405. <https://doi.org/10.1029/12007JB005008>
- Nziengui, J. J. (1993). *Excès d'argon radiogénique dans les quartz des fissures tectoniques: Implication pour la datation des séries métamorphiques, l'exemple de la coupe de la Romanche, Alpes Occidentales* (p. 209). PhD, University Joseph Fourier.
- Paterson, M. S. (1990). Superplasticity in geological materials. *Materials Research Society Symposium Proceedings*, *196*, 303–312.
- Pfiffner, O. A., & Ramsay, J. G. (1982). Constraints on geological rate: Arguments from finite strain values of naturally deformed rocks. *Journal of Geophysical Research*, *87*, 311–321.
- Pluymakers, A., & Spiers, C. J. (2014). Compaction creep of simulated anhydrite fault gouge by pressure solution: Theory vs experiments and implication for fault sealing. In D. R. Faulkner, E. Mariani, & J. Mecklenburgh, (Eds.), *Rock deformation from field, experiments and theory: A volume in honor of Ernie Rutter*. Geological Society, London, Special Publications. <https://doi.org/10.1144/SP1409.1146>
- Poirier, J. P. (1985). *Creep of crystals* (p. 260). Cambridge University Press.
- Putnis, A., & Putnis, C. V. (2007). The mechanism of reequilibration of solids in the presence of a fluid phase. *Journal of Solid State Chemistry*, *180*, 1783–1786.
- Raj, R. (1982). Creep in polycrystalline aggregates by matter transport through a liquid phase. *Journal of Geophysical Research*, *87*, 4731–4739.
- Raj, R., & Chung, C. K. (1981). Solution-precipitation creep in glass ceramics. *Acta Metallurgica*, *29*, 159–166.
- Ramsay, J. G. (1967). *Folding and fracturing of rocks* (p. 568). MacGraw-Hill Book Company.
- Renard, F. (2022). Pressure solution grain boundary sliding as a large deformation mechanism of superplastic flow in the upper crust. [Dataset]. Norstore. <https://doi.org/10.11582/2022.00059>
- Renard, F., Beauprêtre, S., Voisin, C., Zigone, D., Candela, T., Dysthe, D. K., & Gratier, J. P. (2012). Strength evolution of a reactive frictional interface is controlled by the dynamics of contacts and chemical effects. *Earth and Planetary Science Letters*, *341*, 20–34.
- Renard, F., Dysthe, D. K., Feder, J., Bjolykke, K., & Jamtveit, B. (2001). Enhanced pressure solution creep rates induced by clay particles: Experimental evidence in salt aggregates. *Geophysical Research Letters*, *28*(7), 1295–1298.

- Renard, F., Gratier, J. P., & Jamtveit, B. (2000). Kinetics of crack-sealing, intergranular pressure solution and compaction around active faults. *Journal of Structural Geology*, *22*(10), 1395–1407.
- Renard, F., Ortoleva, P., & Gratier, J. P. (1997). Pressure solution in sandstones: Influence of clays and dependence on temperature and stress. *Tectonophysics*, *280*, 257–266.
- Rostom, F., Royne, A., Dysthe, D., & Renard, F. (2013). Effect of fluid salinity on subcritical crack propagation in calcite. *Tectonophysics*, *583*(11), 68–75.
- Ruiz-Agudo, E., Putnis, C. V., & Putnis, A. (2014). Coupled dissolution and precipitation at mineral-fluid interfaces. *Chemical Geology*, *383*, 132–146.
- Rutter, E. H. (1976). The kinetics of rock deformation by pressure solution. *Philosophical Transactions of the Royal Society of London*, *283*, 203–219.
- Rutter, E. H., Casey, M., & Burlini, L. (1994). Preferred crystallographic orientation development during the plastic and superplastic flow of calcite rocks. *Journal of Structural Geology*, *16*(10), 1431–1446.
- Rybacki, E., Wirth, R., & Dresen, G. (2010). Superplasticity and ductile fracture of synthetic feldspar deformed to large strain. *Journal of Geophysical Research*, *115*, B08209. <https://doi.org/10.1029/2009JB007203>
- Saur, H., Sénéchal, P., Boiron, T., Aubourg, C., Derluyn, H., & Moonen, P. (2020). First investigation of quartz and calcite shape fabrics in strained shales by means of X-ray tomography. *Journal of Structural Geology*, *130*, 103905.
- Schenk, O., Urai, J. L., & Evans, B. (2005). The effect of water on recrystallization behavior and grain boundary morphology in calcite—observations of natural marble mylonites. *Journal of Structural Geology*, *27*, 1856–1872.
- Schmid, S. M., Boland, J. N., & Paterson, M. S. (1977). Superplastic flow in fine grained limestone. *Tectonophysics*, *43*, 257–291.
- Sechier, M. (2013). *Geologie et Patrimoine, Matheysine et alentours*. Retrieved from <http://geologie-patrimoine-matheysine.fr>
- Sharma, M. L., & Wason, H. R. (1994). Occurrence of low stress drop earthquakes in the Garhwal Himalaya region. *Physics of the Earth and Planetary Interiors*, *85*, 265–272.
- Sharp, W. E., & Kennedy, G. C. (1965). The system CaO-CO<sub>2</sub>-H<sub>2</sub>O in the two-phase region calcite + aqueous solution. *The Journal of Geology*, *73*, 391–403.
- Smith, D. L., & Evans, B. (1984). Diffusional crack healing in quartz. *Journal of Geophysical Research*, *89*(B6), 4125–4135.
- van den Ende, M. P. A., Niemeijer, A. R., & Spiers, C. J. (2019). Influence of grain boundary structural evolution on pressure solution creep rates. *Journal of Geophysical Research*, *124*(10), 10210–10230.
- van Noort, R., Spiers, C. J., & Peach, C. J. (2007). Effects of orientation on the diffusive properties of fluid-filled grain boundaries during pressure solution. *Physics and Chemistry of Minerals*, *34*, 95–112.
- van Noort, R., Spiers, C. J., & Peach, C. J. (2011). Structure and properties of loaded silica contacts during pressure solution: Impedance spectroscopy measurements under hydrothermal conditions. *Physics and Chemistry of Minerals*, *38*, 501–516.
- van Noort, R., Visser, H. J. M., & Spiers, C. J. (2008). Influence of grain boundary structure on dissolution controlled pressure solution and retarding effects of grain boundary healing. *Journal of Geophysical Research*, *113*, B03201. <https://doi.org/10.1029/2007JB005223>
- Weill, D. F., & Fyfe, W. S. (1964). The solubility of quartz in H<sub>2</sub>O in the range of 1000–4000 bars and 400–500°C. *Geochimica et Cosmochimica Acta*, *28*(8), 1243–1255.
- Weyl, P. K. (1959). Pressure solution and the force of crystallization: A phenomenological theory. *Journal of Geophysical Research*, *64*, 2001–2025.
- Wintsch, R. P., & Keewook, Y. (2002). Dissolution and replacement creep: A significant deformation mechanism in mid-crustal rocks. *Journal of Structural Geology*, *24*, 1179–1193.
- Zhang, X., & Spiers, C. J. (2005). Effects of phosphate ions on intergranular pressure solution in calcite: An experimental study. *Geochimica et Cosmochimica Acta*, *69*(24), 5681–5691.
- Zhang, X., Spiers, C. J., & Peach, C. J. (2010). Compaction creep of wet granular calcite by pressure solution at 28 °C to 150 °C. *Journal of Geophysical Research*, *115*, B09217.
- Zhang, X., Spiers, C. J., & Peach, C. J. (2011). Effects of pore fluid flow and chemistry on compaction creep of calcite by pressure solution at 150°C. *Geofluids*, *11*(1), 108–122.
- Zoback, M., Hickman, S. H., & Ellsworth, W. (2010). Scientific drilling into the San Andreas fault zone. *Eos, Transactions, American Geophysical Union*, *91*, 197–199.
- Zubtsov, S. F., Renard, F., Gratier, J. P., Guiguet, R., Dysthe, D. K., & Traskine, V. (2004). Experimental pressure solution creep of polymineralic aggregates. *Tectonophysics*, *385*, 45–47.